

Publications scientifiques

Article 1 :

Publié dans la revue *Archive of Applied Mechanics*.

- **Éditeur :** Springer Nature
- **ISSN :** 0939-1533 **E-ISSN :** 1432-0681
- **Période de couverture par Scopus :** de 1991 à 2025
- **Domaine scientifique :** Génie civile et mécanique
- **Type de source :** Revue classée A (*lien* : https://www.dgrsdt.dz/fr/revues_A?search=ARCHIVE+OF+APPLIED+MECHANICS)



وزارة التعليم العالي والبحث العلمي

The screenshot shows the official website of the National Research Agency (DGRSDT). The header includes the logo of the National Research Agency (RS DT) and links for Accueil, DGRSDT, Activités R&D, DEV_TECH, Revues scientifiques, Services, Contact, and APPELS. The main banner features the text "Revues scientifiques de catégorie A". Below the banner, there is a search bar with the placeholder "Rechercher" and a link "Accueil → revues_A".

The screenshot shows the article page for "Static, free vibration, and buckling analysis of functionally graded plates using the strain-based finite element formulation" published in the *Archive of Applied Mechanics*. The page includes author information (Taqiyeddine Assas, Messaoud Bourezane, Madja Chenafi), access metrics (350 accesses, 6 citations), and links for "Access this article" and "Log in via an institution".

Original | Published: 06 July 2024
Volume 94, pages 2243–2267, (2024) [Cite this article](#)

[Archive of Applied Mechanics](#)

[Aims and scope](#) →
[Submit manuscript](#) →

Taqiyeddine Assas [✉](#), Messaoud Bourezane & Madja Chenafi

350 Accesses 6 Citations [Explore all metrics](#) →

Access this article

Log in via an institution →



ORIGINAL

Taqiyeddine Assas · Messaoud Bourezane · Madjda Chenafi

Static, free vibration, and buckling analysis of functionally graded plates using the strain-based finite element formulation

Received: 13 February 2024 / Accepted: 15 June 2024

© The Author(s), under exclusive licence to Springer-Verlag GmbH Germany, part of Springer Nature 2024

Abstract In the current investigation, the novelty lies in the formulation of a novel four-node rectangular finite element with six degrees of freedom per node using the strain approach and first-order shear deformation theory, therefore, this is the first article to use this approach to analyze the static, free vibration, and buckling behaviors of functionally graded. The properties of FGM vary continuously through the thickness direction according to the volume fraction of constituents defined by a simple power law function. The notion of a neutral surface is presented to prevent membrane bending coupling. The displacement functions of the suggested element which possess higher-order expressions, is based on assumed functions of strain that satisfy both rigid body modes and compatibility equations. The performance of the developed element is verified and compared with the published results in the literature and excellent agreement is observed. The influence of the geometrical, material properties, and loading types with different boundary conditions on the bending, free vibration, and buckling analysis of FGM plate are also studied and discussed for the first time using the strain-based finite element formulation.

Keywords Static · Free vibration · Buckling · Reissner–Mindlin · Functionally graded · Strain approach

1 Introduction

Functionally graded materials (FGM) are new composite materials that were initially developed in 1984 by a team of researchers in Japan. They are commonly composed of a combination of ceramic and metal. The properties of FGM change continuously and smoothly from one face to the other and therefore avoid the interfacial stress concentration observed in laminated composites. These novel materials were first proposed as ways to produce a thermal barrier material because of their ductility given by the metal component and high temperature resistance from the ceramic component [1]. FGM is developed for application in different industries and engineering disciplines. Therefore, due to their excellent properties, several authors have been motivated to investigate their static, free vibrational and buckling responses by applying different analytical and numerical approaches based on different theories, including the first-order shear deformation theory (FSDT) and the higher-order shear deformation theory (HSDT). For the first one, Reddy [2] analyzed the bending analysis of functionally graded (FG) plates using third-order shear deformation plate theory (TSDT). Zenkour [3] proposed an analytical results for the bending behavior of composite plates exposed to thermo-mechanic loading based on the HSDT. Vel and Batra [4, 5] introduced a three-dimensional (3D) precise model for analyzing thermo-mechanical deformations and forced vibrations in FG rectangular plates. Matsunaga [6] analyzed the fundamental frequency and buckling stress of FG plates using the two-dimensional (2D) HSDT.

T. Assas (✉) · M. Bourezane · M. Chenafi

Laboratory of Hydraulic Developments and Environment (LAHE), Civil Engineering and Hydraulic Department, University of Biskra, Biskra, Algeria
e-mail: taqiyeddine.assas@univ-biskra.dz

Nguyen-Xuan et al. [7] applied the strain smoothing method to analyze the static, free vibrational, and thermo-mechanical buckling behaviors of FG plates employing FSDT. Mantari et al. [8] studied the free vibration behavior of FG plates supported on an elastic foundation using a new non-polynomial HSDT. Bellifa et al. [9] examined the bending and free vibrational characteristics of FG plates using a simple FSDT approach that considers neutral surface position. Zaoui et al. [10] investigated the free vibration analysis of FG plates resting on Pasternak elastic foundations using a 2D and quasi three-dimensional (quasi-3D) HSDT.

Recently, Tati [11] developed a four nodes finite element with five unknowns using the HSDT for the bending characteristics of FG rectangular plates exposed to uniform and sinusoidal lateral loads. In a different study, Tati [12] used his finite element model [11] to examine thermo-mechanical buckling behavior. Sadgui and Tati [13] introduced novel sinusoidal shear function to analyze the free vibration and stability characteristics of FGM plates, utilizing the HSDT. Belouar et al. [14, 15] developed a novel quadrilateral finite element incorporating the assumed strain technique to analyze the bending, free vibrational, and buckling characteristics of FG square, skew, and circular plates, based on the FSDT.

Nowadays, the finite element method (FEM) has been proved to be a powerful and reliable computational tool for the analysis of FG ultra-small structures such as FG nanobeams, microbeams, and microplates. Several numerical models based on the FEM have been proposed by many researchers to predict accurately the behavior of FG nanostructures and microstructures. Cuong et al. [16] used for the first time the modified HSDT type hyperbolic sine functions theory and the FEM to study the static bending response of rotating functionally graded GPL-reinforced composite (FG-GPLRC) beams with initial geometrical deficiencies in thermal media. Belabed et al. [17] formulated a novel beam finite element model with only three degrees of freedom (DoFs) for the buckling and free vibration responses of FG porous beams supported by Winkler-Pasternak elastic foundations. In a separate study, Belabed et al. [18] presented an enhanced finite element beam model aimed at assessing the dynamic characteristics of FG sandwich beams with variable cross-sections. Based on the FSDT, free vibration analysis of FGM sandwich plates with porosity was studied by Bentrar et al. [19] using the p-version of the FEM. Tien et al. [20] studied the issue of forced vibration and buckling in organic nanoplates using nonlocal theory and a variety of deformation plate theories. Mesbah et al. [21] proposed a new FEM based on simple HSDT for the free vibration and buckling behaviors of FG porous beams. Xia et al. [22] used the FEM to investigate the dynamic of FG porous truncated conical panels reinforced with graphene platelets (GPLs) based on the 3D elasticity. Civalek et al. [23] investigated the static and free torsional vibration of FG nanorods using the Fourier sine series. In another study, Civalek et al. [24] presented the stability analysis of nanobeams under the influence of electromagnetic fields using FEM. Additionally, Civalek et al. [25] solved the bending, buckling, and vibration problems of Euler-Bernoulli nanobeams with various cross-sections based on nonlocal elasticity theory. Ebrahimi and Reza Barati [26] explored the thermal vibration characteristics of FG nanobeams based on TSVD under different thermo-mechanical loading conditions. Uzun and Yayli [27] examined the free vibrational frequencies of constrained nonlocal Rayleigh nanobeams made of FGM, characterized by four different porosity distributions. Demir and Civalek [28] proposed a new nonlocal FEM using Hermitian cubic shape functions for the thermal vibration analysis of nanobeams surrounded by an elastic matrix. Akgöz and Civalek [29] investigated the vibration response of non-homogeneous and non-uniform microbeams using the Bernoulli-Euler beam theory coupled with the modified couple stress theory.

Various researchers have utilized the strain approach to construct efficient and study finite elements. Ashwell et al. [30] were the first to develop such elements specifically for handling curved problems. Then, this approach was applied to plane elasticity elements [31–33] and then extended to 3D elasticity problems [34–36], for plate bending [37–42], and shell structures [43–45]. It can be observed that all existing strain-based plate elements were designed for only isotropic materials and this has motivated the authors to develop a new strain-based finite element for analyzing FG plates.

The objective of this paper is to evaluate the performance of the strain approach to develop a novel four-node rectangular element based on Reissner-Mindlin plate theory to investigate for the first time the static, free vibration and buckling behaviors of FG plates. The properties of FGM vary progressively along the thickness direction as a function of the volume fraction of the components, which are defined by a simple power-law function. The proposed element, called SBRMP24 (Strain-Based Rectangular Mindlin Plate with 24 unknowns), possesses six degrees of freedom (DOFs) ($u, v, \theta_z, w, \beta_x, \beta_y$) for each node. The displacement functions of the suggested element which possess higher-order expressions, is based on assumed functions of strain that satisfy both rigid body modes and compatibility equations. Additionally, the potential energy and the principle of Hamilton are applied to obtain the rigidity, mass, and geometrical matrices. Different numerical examples are studied and analyzed to demonstrate the performance of the current finite element model in predicting the static, free vibrational, and buckling behaviors of the FG plates.

2 Mathematical formulation

2.1 Displacement functions and strains

The displacement terms of a plate, on the basis of the simple FSDT, can be formulated as [46]:

$$\begin{aligned} U(x, y, z) &= u(x, y) + z\beta_x(x, y) \\ V(x, y, z) &= v(x, y) + z\beta_y(x, y) \\ W(x, y, z) &= w(x, y) \\ \theta_z(x, y, z) &= \theta_z(x, y) \end{aligned} \quad (1)$$

U, V , and W are the displacements of each point of the coordinates (x, y, z) ; u, v are the in-plane displacement vector components at any point of the neutral surface in x and y directions, respectively.

$w(x, y)$ is the transverse displacement of neutral surface points of the plate. β_x, β_y and θ_z are the rotation of the normal to the yz , xz and xy planes, respectively.

Where the drilling rotation θ_z is defined by the following [47]:

$$\theta_z(x, y) = \frac{1}{2} \left(\frac{\partial v(x, y)}{\partial x} - \frac{\partial u(x, y)}{\partial y} \right) \quad (2)$$

The displacement and strain components are related by the following relationships [12]:

$$\{\varepsilon\} = \begin{Bmatrix} \varepsilon_x \\ \varepsilon_y \\ \gamma_{xy} \end{Bmatrix} = \begin{Bmatrix} \varepsilon_x^l \\ \varepsilon_y^l \\ \gamma_{xy}^l \end{Bmatrix} + \begin{Bmatrix} \varepsilon_x^{nl} \\ \varepsilon_y^{nl} \\ \gamma_{xy}^{nl} \end{Bmatrix} \quad (3)$$

$$\{\varepsilon^l\} = \begin{Bmatrix} \varepsilon_x^l \\ \varepsilon_y^l \\ \gamma_{xy}^l \end{Bmatrix} = \{\varepsilon^m\} + z\{\kappa\} = \begin{Bmatrix} \varepsilon_x^m \\ \varepsilon_y^m \\ \gamma_{xy}^m \end{Bmatrix} + z \begin{Bmatrix} \kappa_x \\ \kappa_y \\ \kappa_{xy} \end{Bmatrix} \quad (4)$$

$$\{\gamma\} = \begin{Bmatrix} \gamma_{xz} \\ \gamma_{yz} \end{Bmatrix} \quad (5)$$

where

$$\{\varepsilon^m\} = \begin{Bmatrix} \varepsilon_x^m \\ \varepsilon_y^m \\ \gamma_{xy}^m \end{Bmatrix} = \begin{Bmatrix} \frac{\partial u}{\partial x} \\ \frac{\partial v}{\partial y} \\ \left(\frac{\partial u}{\partial y} + \frac{\partial v}{\partial x} \right) \end{Bmatrix} \quad (6)$$

$$\{\kappa\} = \begin{Bmatrix} \kappa_x \\ \kappa_y \\ \kappa_{xy} \end{Bmatrix} = \begin{Bmatrix} \frac{\partial \beta_x}{\partial x} \\ \frac{\partial \beta_y}{\partial y} \\ \left(\frac{\partial \beta_x}{\partial y} + \frac{\partial \beta_y}{\partial x} \right) \end{Bmatrix} \quad (7)$$

$$\{\varepsilon^{nl}\} = \begin{Bmatrix} \varepsilon_x^{nl} \\ \varepsilon_y^{nl} \\ \gamma_{xy}^{nl} \end{Bmatrix} = \begin{Bmatrix} \frac{1}{2} \left(\frac{\partial w}{\partial x} \right)^2 \\ \frac{1}{2} \left(\frac{\partial w}{\partial y} \right)^2 \\ \left(\frac{\partial w}{\partial x} \frac{\partial w}{\partial y} \right) \end{Bmatrix} \quad (8)$$

$$\{\gamma\} = \begin{Bmatrix} \gamma_{xz} \\ \gamma_{yz} \end{Bmatrix} = \begin{Bmatrix} \frac{\partial w}{\partial x} + \beta_x \\ \frac{\partial w}{\partial y} + \beta_y \end{Bmatrix} \quad (9)$$

where $\{\varepsilon^m\}$, $\{\kappa\}$ and $\{\varepsilon^{nl}\}$ are membrane, bending and the nonlinear strains vectors, respectively. $\{\gamma\}$ is the transverse shear strain vector.

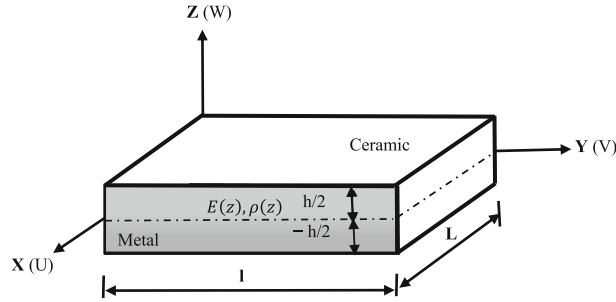


Fig. 1 Geometry of rectangular FGM plate

2.2 Constitutive relations

The plate is formed from a blend of ceramic and metal materials at the upper and lower surfaces, respectively, as shown in Fig. 1. The properties of the two materials are progressively graded across the thickness using the following power-law function [10, 48]:

$$P(z) = P_m + (P_c - P_m) \left(\frac{z}{h} + \frac{1}{2} \right)^p \quad (10)$$

where m and c symbols represent the metal and ceramic, respectively. P_c and P_m are the associated material characteristics, such as density (ρ), Young's modulus (E), and other various characteristics. ($p \geq 0$) is the gradient index.

The constitutive expressions for the elastic FGM plate are defined by [11]:

$$\begin{Bmatrix} \sigma_x \\ \sigma_y \\ \tau_{xy} \end{Bmatrix} = \begin{bmatrix} D_{11} & D_{12} & 0 \\ D_{21} & D_{22} & 0 \\ 0 & 0 & D_{66} \end{bmatrix} \begin{Bmatrix} \varepsilon_x^l \\ \varepsilon_y^l \\ \gamma_{xy}^l \end{Bmatrix} \quad (11)$$

or

$$\{\sigma\} = [D_\sigma] \{\varepsilon^l\} \quad (12)$$

$$\begin{Bmatrix} \tau_{xz} \\ \tau_{yz} \end{Bmatrix} = \begin{bmatrix} D_{44} & 0 \\ 0 & D_{55} \end{bmatrix} \begin{Bmatrix} \gamma_{xz} \\ \gamma_{yz} \end{Bmatrix} \quad (13)$$

or

$$\{\tau\} = [D_\tau] \{\gamma\} \quad (14)$$

where $(\sigma_x, \sigma_y, \tau_{xy}, \tau_{xz}, \tau_{yz})$ and $(\varepsilon_x, \varepsilon_y, \gamma_{xy}, \gamma_{xz}, \gamma_{yz})$ are the stresses and strains, respectively. The rigidity coefficients D_{ij} can be formulated according to the material properties given in Eq. (10) as follows:

$$\begin{aligned} D_{11} &= D_{22} = \frac{E(z)}{1 - \nu^2}; \\ D_{12} &= D_{21} = \nu \frac{E(z)}{1 - \nu^2}, \\ D_{44} &= D_{55} = D_{66} = \frac{E(z)}{2(1 + \nu)} \end{aligned} \quad (15)$$

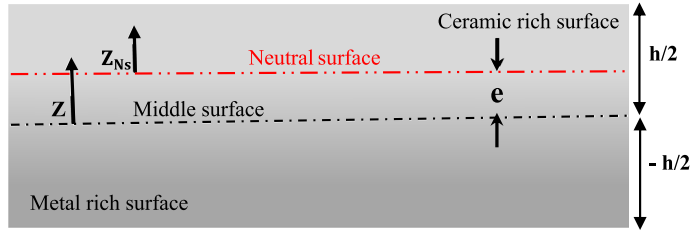


Fig. 2 Location of the neutral surface of FGM plate

2.3 Stress resultants

To prevent the coupling of the stretching and bending effects produced by the asymmetric material characteristics of functionally graded plates with respect to the central surface, the force and moments are determined using the neutral surface position z_{Ns} , which is not coincident with the central surface of the plate, as illustrated in Fig. 2 [11, 13].

$$z_{Ns} = z - e \quad (16)$$

The neutral surface position can be found by selecting (e) so that the membrane force resulting from bending at the level of ($z = e$) must be zero [13].

$$\left\{ \int_{-\frac{h}{2}}^{\frac{h}{2}} \sigma_x dz_{Ns} = \int_{-\frac{h}{2}}^{\frac{h}{2}} \left[D_{11}(z - e) \frac{\partial \beta_x}{\partial x} + D_{12}(z - e) \frac{\partial \beta_y}{\partial y} \right] dz = 0 \right\} \quad (17)$$

By replacing Eq. (15) into Eq. (17), we obtain:

$$\int_{-\frac{h}{2}}^{\frac{h}{2}} \left[\frac{E(z)}{1 - \nu^2} (z - e) \frac{\partial \beta_x}{\partial x} + \nu \frac{E(z)}{1 - \nu^2} (z - e) \frac{\partial \beta_y}{\partial y} \right] dz = 0 \quad (18)$$

Simplifying Eq. (18), we get:

$$\frac{1}{1 - \nu^2} \left(\frac{\partial \beta_x}{\partial x} + \nu \frac{\partial \beta_y}{\partial y} \right) \int_{-\frac{h}{2}}^{\frac{h}{2}} (E(z)(z - e)) dz = 0 \quad (19)$$

Then,

$$\int_{-\frac{h}{2}}^{\frac{h}{2}} (E(z)(z - e)) dz = 0, \quad \int_{-\frac{h}{2}}^{\frac{h}{2}} E(z)z dz - (e) \int_{-\frac{h}{2}}^{\frac{h}{2}} E(z) dz = 0 \quad (20)$$

Consequently, the neutral surface's position can be established as [12, 49]:

$$e = \frac{\int_{-h/2}^{h/2} E(z)z dz}{\int_{-h/2}^{h/2} E(z) dz} \quad (21)$$

The membrane $\{N\}$, bending $\{M\}$ and shear $\{T\}$ stress resultants are calculated by using the neutral surface position as [12, 13]:

$$\begin{aligned} \begin{Bmatrix} N_x \\ N_y \\ N_{xy} \end{Bmatrix} &= \int_{-h/2}^{h/2} \begin{Bmatrix} \sigma_x(z) \\ \sigma_y(z) \\ \tau_{xy}(z) \end{Bmatrix} dz; \quad \begin{Bmatrix} M_x \\ M_y \\ M_{xy} \end{Bmatrix} = \int_{-h/2}^{h/2} \begin{Bmatrix} \sigma_x(z) \\ \sigma_y(z) \\ \tau_{xy}(z) \end{Bmatrix} (z - e) dz; \\ \begin{Bmatrix} T_x \\ T_y \end{Bmatrix} &= \int_{-h/2}^{h/2} \begin{Bmatrix} \tau_{xz} \\ \tau_{yz} \end{Bmatrix} dz \end{aligned} \quad (22)$$

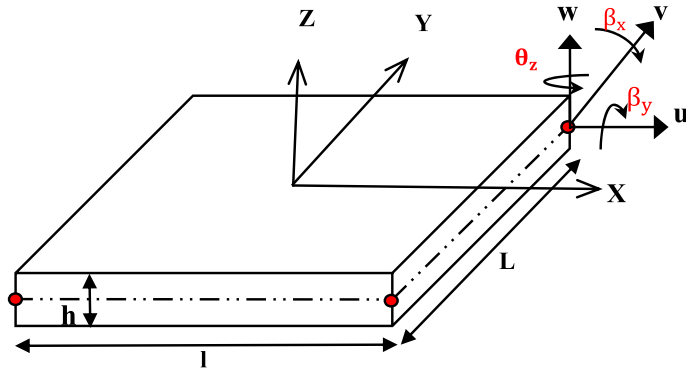


Fig. 3 Rectangular plate element (SBRMP24)

The relationship of the resulting stresses and strains may be formulated as follows:

$$\begin{Bmatrix} N \\ M \\ T \end{Bmatrix} = \begin{bmatrix} [D_m] & 0 & 0 \\ 0 & [D_b] & 0 \\ 0 & 0 & [D_s] \end{bmatrix} \begin{Bmatrix} \varepsilon^m \\ \kappa \\ \gamma \end{Bmatrix} \quad (23)$$

where the constitutive matrices for membrane $[D_m]$, bending $[D_b]$, and shear $[D_s]$ are given by [11, 12]:

$$[D_m] = \int_{-h/2}^{h/2} [D_\sigma] dz; \quad [D_b] = \int_{-h/2}^{h/2} [D_\sigma](z - e)^2 dz; \quad [D_s] = k_s \int_{-h/2}^{h/2} [D_\tau] dz \quad (24)$$

where $k_s = \frac{5}{6}$ is shear correction factor.

3 Finite element formulation

The formulated rectangular plate element SBRMP24 contains six DOFs ($u, v, \theta_z, w, \beta_x, \beta_y$) for each node, as shown in Fig. 3. Their displacement expressions are derived by combining two assumed strain elements. The first one is a membrane element suggested by Sabir [33], which has three DOFs (u, v, θ_z) for each node. The second one, a bending element based on the FSDT with three DOFs (w, β_x, β_y) for each node, was introduced by Belounar et al. [39].

3.1 Displacements field of current element (SBRMP24)

The displacements field, as presented in reference [33], for the membrane element is as follows:

$$\begin{Bmatrix} u \\ v \\ \theta_z \end{Bmatrix} = [P_m]\{\alpha_m\} \quad (25)$$

where the matrix function of membrane element $[P_m]$ is given by [33]:

$$[P_m] = \begin{bmatrix} 1 & 0 & -y & x & xy & 0 & 0 & \frac{y}{2} & 0 & \frac{y^2}{2} & xy^2 & x^2y^3 \\ 0 & 1 & x & 0 & 0 & y & xy & \frac{x}{2} & \frac{x^2}{2} & 0 & -x^2y & -x^3y^2 \\ 0 & 0 & 1 & 0 & -\frac{x}{2} & 0 & \frac{y}{2} & 0 & \frac{x}{2} & -\frac{y}{2} & -2xy & -3x^2y^2 \end{bmatrix} \quad (26)$$

And $\{\alpha_m\} = \{\alpha_1, \alpha_2, \dots, \alpha_{12}\}^T$.

The displacement functions for bending plate element as described in reference [39] are:

$$\begin{Bmatrix} w \\ \beta_x \\ \beta_y \end{Bmatrix} = [P_b]\{\alpha_b\} \quad (27)$$

where $\{\alpha_b\} = \{\alpha_{13}, \alpha_2, \dots, \alpha_{24}\}^T$.

Where the matrix function of bending plate element $[P_b]$ is given by [39]:

$$[P_b] = \begin{bmatrix} 1 & -x & -y & -\frac{x^2}{2} & -\left(\frac{x^2y}{2} + \frac{y^3}{12}\right) & -\frac{y^2}{2} & -\left(\frac{xy^2}{2} + \frac{x^3}{12}\right) & -\frac{xy}{2} & \frac{x}{2} & \frac{xy}{2} & \frac{y}{2} & \frac{xy}{2} \\ 0 & 1 & 0 & x & xy & 0 & \left(\frac{x^2}{4} + \frac{y^2}{2}\right) & \frac{y}{2} & \frac{1}{2} & \frac{y}{2} & 0 & -\frac{y}{2} \\ 0 & 0 & 1 & 0 & \left(\frac{y^2}{4} + \frac{x^2}{2}\right) & y & xy & \frac{x}{2} & 0 & -\frac{x}{2} & \frac{1}{2} & \frac{x}{2} \end{bmatrix} \quad (28)$$

As mentioned above, the displacement field for the current element (SBRMP24) may be obtained by combining Eqs. (26), (28), which are based on assumed functions of strain that satisfy both rigid body modes and compatibility equations (“Appendix”). The expressions can be represented in relation to the twenty-four constants ($\{\alpha\}^T = (\alpha_1, \alpha_2, \dots, \alpha_{24})$) as:

$$\{U_e\} = \begin{Bmatrix} u \\ v \\ \theta_z \\ w \\ \beta_x \\ \beta_y \end{Bmatrix} = \begin{bmatrix} [P_m] & [0]_{(3 \times 12)} \\ [0]_{(3 \times 12)} & [P_b] \end{bmatrix} \begin{Bmatrix} \{\alpha_m\} \\ \{\alpha_b\} \end{Bmatrix} = [P]\{\alpha\} \quad (29)$$

where $\{\alpha\}^T = \{\{\alpha_m\}\{\alpha_b\}\}^T = \{\alpha_1, \dots, \alpha_{24}\}^T$

$$[P] = \begin{bmatrix} [P_m] & [0]_{(3 \times 12)} \\ [0]_{(3 \times 12)} & [P_b] \end{bmatrix} \quad (30)$$

The transformation matrix $[C]$ that connects the 24 DOFs ($\{q_e\}^T = \{u_i, v_i, \theta_{zi}, w_i, \beta_{xi}, \beta_{yi}\}_{i=1,2,3,4}$) to the 24 constants ($\{\alpha\}^T = (\alpha_1, \alpha_2, \dots, \alpha_{24})$) can be expressed as:

$$\{q_e\} = [C]\{\alpha\} \quad (31)$$

where

$$[C] = \{[P_1] \quad [P_2] \quad [P_3] \quad [P_4]\}^T \quad (32)$$

And the matrices $[P_i]$ (for x_i, y_i from node i ($i = 1, 2, 3$, and 4)) are described using the expression provided in Eq. (30):

$$[P_i] = \begin{bmatrix} [P_m]_i & 0 \\ 0 & [P_b]_i \end{bmatrix}_{\text{node}, i=1,2,3,4} \quad (33)$$

Using Eq. (31), we can now determine the constant values vector $\{\alpha\}$.

$$\{\alpha\} = [C]^{-1}\{q_e\} \quad (34)$$

Then, by replacing Eq. (34) into Eq. (29), we get:

$$\{U_e\} = \begin{Bmatrix} u \\ v \\ \theta_z \\ w \\ \beta_x \\ \beta_y \end{Bmatrix} = [P][C]^{-1}\{q_e\} = [N]\{q_e\} \quad (35)$$

where

$$[N] = [P][C]^{-1} \quad (36)$$

3.2 Strain–displacement relations

The membrane strains $\{\varepsilon^m\}$ are calculated using Eq. (6):

$$\{\varepsilon^m\} = \begin{Bmatrix} \varepsilon_x^m \\ \varepsilon_y^m \\ \gamma_{xy}^m \end{Bmatrix} = \begin{bmatrix} \frac{\partial}{\partial x} & 0 & 0 \\ 0 & \frac{\partial}{\partial y} & 0 \\ \frac{\partial}{\partial y} & \frac{\partial}{\partial x} & 0 \end{bmatrix} \begin{Bmatrix} u \\ v \\ \theta_z \end{Bmatrix} \quad (37)$$

By replacing Eq. (29) into Eq. (37), we obtain:

$$\{\varepsilon^m\} = \begin{bmatrix} \frac{\partial}{\partial x} & 0 & 0 \\ 0 & \frac{\partial}{\partial y} & 0 \\ \frac{\partial}{\partial y} & \frac{\partial}{\partial x} & 0 \end{bmatrix} [[P_m][0]_{3 \times 12}]_{3 \times 24} \{\alpha\} = [Q_m]\{\alpha\} \quad (38)$$

where the membrane strains matrix $[Q_m]$ is given by:

$$[Q_m] = \begin{bmatrix} 0 & 0 & 0 & 1 & y & 0 & 0 & 0 & 0 & y^2 & 2xy^3 & 0 & 0 & 0 & 0 & 0 & 0 & 0 & 0 & 0 & 0 & 0 & 0 & 0 & 0 \\ 0 & 0 & 0 & 0 & 0 & 1 & x & 0 & 0 & 0 & -x^2 & -2x^3y & 0 & 0 & 0 & 0 & 0 & 0 & 0 & 0 & 0 & 0 & 0 & 0 & 0 & 0 \\ 0 & 0 & 0 & 0 & x & 0 & y & 1 & x & y & 0 & 0 & 0 & 0 & 0 & 0 & 0 & 0 & 0 & 0 & 0 & 0 & 0 & 0 & 0 & 0 \end{bmatrix} \quad (39)$$

Using Eqs. (7), (9), the curvatures and shear strains-displacements relationship given by:

$$\{\kappa\} = \begin{Bmatrix} \kappa_x \\ \kappa_y \\ \kappa_{xy} \end{Bmatrix} = \begin{bmatrix} 0 & \frac{\partial}{\partial x} & 0 \\ 0 & 0 & \frac{\partial}{\partial y} \\ 0 & \frac{\partial}{\partial y} & \frac{\partial}{\partial x} \end{bmatrix} \begin{Bmatrix} w \\ \beta_x \\ \beta_y \end{Bmatrix} \quad (40)$$

$$\{\gamma\} = \begin{Bmatrix} \gamma_{xz} \\ \gamma_{yz} \end{Bmatrix} = \begin{bmatrix} \frac{\partial}{\partial x} & 1 & 0 \\ \frac{\partial}{\partial y} & 0 & 1 \end{bmatrix} \begin{Bmatrix} w \\ \beta_x \\ \beta_y \end{Bmatrix} \quad (41)$$

Substitution of Eq. (29) in Eq. (40) and Eq. (41), we obtain:

$$\{\kappa\} = \begin{bmatrix} 0 & \frac{\partial}{\partial x} & 0 \\ 0 & 0 & \frac{\partial}{\partial y} \\ 0 & \frac{\partial}{\partial y} & \frac{\partial}{\partial x} \end{bmatrix} [[0]_{3 \times 12} \ [P_b]]_{3 \times 24} \{\alpha\} = [Q_b]\{\alpha\} \quad (42)$$

$$\{\gamma\} = \begin{bmatrix} \frac{\partial}{\partial x} & 1 & 0 \\ \frac{\partial}{\partial y} & 0 & 1 \end{bmatrix} [[0]_{3 \times 12} \ [P_b]]_{3 \times 24} \{\alpha\} = [Q_s]\{\alpha\} = [Q_s]\{\alpha\} \quad (43)$$

where the bending $[Q_b]$ and the transverse shear $[Q_s]$ strains matrices are:

$$[Q_b] = \begin{bmatrix} 0 & 0 & 0 & 0 & 0 & 0 & 0 & 0 & 0 & 0 & 0 & 0 & 0 & 0 & 0 & 1 & y & 0 & \frac{x}{2} & 0 & 0 & 0 & 0 & 0 & 0 \\ 0 & 0 & 0 & 0 & 0 & 0 & 0 & 0 & 0 & 0 & 0 & 0 & 0 & 0 & 0 & 0 & \frac{y}{2} & 1 & x & 0 & 0 & 0 & 0 & 0 & 0 & 0 \\ 0 & 0 & 0 & 0 & 0 & 0 & 0 & 0 & 0 & 0 & 0 & 0 & 0 & 0 & 0 & 0 & (2x) & 0 & (2y) & 1 & 0 & 0 & 0 & 0 & 0 \end{bmatrix} \quad (44)$$

$$[Q_s] = \begin{bmatrix} 0 & 0 \\ 0 & 0 \end{bmatrix} \quad (45)$$

The geometric strains can be formulated as [15]:

$$\{\varepsilon^g\} = \begin{Bmatrix} \frac{\partial W}{\partial x} \\ \frac{\partial W}{\partial y} \end{Bmatrix} \quad (46)$$

Substituting the transverse displacement (w) of Eq. (29) into Eq. (46) gives:

$$\{\varepsilon^g\} = [G]\{\alpha\} \quad (47)$$

where

$$[G] = \begin{bmatrix} 0 & 0 & 0 & 0 & 0 & 0 & 0 & 0 & 0 & 0 & -1 & 0 & -x & -xy & 0 & -\left(\frac{y^2}{2} + \frac{x^2}{4}\right) & -\frac{y}{2} & \frac{1}{2} & \frac{y}{2} & 0 & \frac{y}{2} \\ 0 & 0 & 0 & 0 & 0 & 0 & 0 & 0 & 0 & 0 & -1 & 0 & -\left(\frac{x^2}{2} + \frac{y^2}{4}\right) & -y & -xy & -\frac{x}{2} & 0 & \frac{x}{2} & \frac{1}{2} & \frac{x}{2} \end{bmatrix} \quad (48)$$

The strains- displacements relationship are obtained by replacing Eq. (34) into Eqs. (38, 42, 43, and 47), to have:

$$\{\varepsilon^m\} = [Q_m][C]^{-1}\{q_e\} = [B_m]\{q_e\} \quad (49)$$

$$\{\kappa\} = [Q_b][C]^{-1}\{q_e\} = [B_b]\{q_e\} \quad (50)$$

$$\{\gamma\} = [Q_s][C]^{-1}\{q_e\} = [B_s]\{q_e\} \quad (51)$$

$$\{\varepsilon^g\} = [G][C]^{-1}\{q_e\} = [B_g]\{q_e\} \quad (52)$$

where $[B_m]$, $[B_b]$, $[B_s]$, and $[B_g]$ represent strain displacement matrices given by:

$$[B_m] = [Q_m][C]^{-1}; [B_b] = [Q_b][C]^{-1}; [B_s] = [Q_s][C]^{-1}; [B_g] = [G][C]^{-1} \quad (53)$$

3.3 Deduction of the elementary matrices

The stiffness and geometrical matrices are obtained by applying the total potential energy:

$$\pi = U - W \quad (54)$$

where U and W are respectively the strain potential energy and the work done due to external force with respect to the neutral plane Z_{Ns} .

The strain potential energy is given by [11, 50]:

$$U = \frac{1}{2} \int_V \left(\{\varepsilon'\}^T \{\sigma\} + \{\gamma\}^T \{\tau\} \right) dV = \frac{1}{2} \int_V \left(\{\varepsilon^m\}^T \{\sigma\} + z\{\kappa\}^T \{\sigma\} + \{\gamma\}^T \{\tau\} \right) dV \quad (55)$$

By integrating across the thickness and using Eq. (22); Eq. (55) can be reformulated as [13]:

$$U = \frac{1}{2} \int_{\Omega} \left(\{\varepsilon^m\}^T \{N\} + \{\kappa\}^T \{M\} + \{\gamma\}^T \{T\} \right) d\Omega \quad (56)$$

Substituting Eqs. (23), (49), (50), and Eq. (51) into the above equation to obtain:

$$U = \frac{1}{2} \int_{\Omega} \left(\{q_e\}^T \left([B_m]^T [D_m] [B_m] + [B_b]^T [D_b] [B_b] \right. \right. \\ \left. \left. + [B_s]^T [D_s] [B_s] \right) \{q_e\} \right) d\Omega \quad (57)$$

where V and Ω are the volume and the top surface of the plate, respectively.

3.3.1 Static analysis

For static analysis, the external work done by the distributed transverse load $q(x, y)$ applied to the FGM plate can be given by [11, 50]:

$$W = \int_{\Omega} w(x, y)q(x, y)d\Omega \quad (58)$$

Inserting Eq. (35) in Eq. (58), we have:

$$W = \int_{\Omega} \{q_e\}^T [N]^T q(x, y)d\Omega \quad (59)$$

Substitution Eqs. (57), (59) in Eq. (54) we have:

$$\begin{aligned} \pi = & \frac{1}{2} \int_{\Omega} \left(\{q_e\}^T \left([B_m]^T [D_m] [B_m] + [B_b]^T [D_b] [B_b] + [B_s]^T [D_s] [B_s] \right) \{q_e\} \right) \\ & - \int_{\Omega} \{q_e\}^T [N]^T q(x, y)d\Omega \end{aligned} \quad (60)$$

For linear bending behavior, the equation of equilibrium can be formulated as follows:

$$[K_e]\{q_e\} = \{F_e\} \quad (61)$$

where $[K_e]$ is the element stiffness matrix and $\{F_e\}$ is the element nodal forces vector given by:

$$[K_e] = \int \left(\underbrace{[B_m]^T [D_m] [B_m]}_{\text{Membrane}} + \underbrace{[B_b]^T [D_b] [B_b]}_{\text{Bending}} + \underbrace{[B_s]^T [D_s] [B_s]}_{\text{Shear}} \right) d\Omega \quad (62)$$

$$\{F_e\} = \int [N]^T q(x, y)d\Omega \quad (63)$$

3.3.2 Free vibration behavior

The mass matrix is obtained by using Hamilton's principle [28]:

$$\delta \int_0^t [T - (U - W)]dt = 0 \quad (64)$$

where T is the kinetic energy of the FGM described as follows [13]:

$$T = \frac{1}{2} \int_{\Omega} \int_{-\frac{h}{2}}^{\frac{h}{2}} \rho(z) \left[(\dot{U})^2 + (\dot{V})^2 + (\dot{W})^2 \right] d\Omega \quad (65)$$

By replacing Eq. (1) in the above equation, we obtain:

$$T = \frac{1}{2} \int \left(I_0((\dot{u})^2 + (\dot{v})^2 + (\dot{w})^2) + I_2((\dot{\beta}_x)^2 + (\dot{\beta}_y)^2) \right) dz \quad (66)$$

where the terms $\rho(z)$ and I_0 , I_2 represent the mass density and moments of inertia, respectively, which are defined as follows [13]:

$$(I_0, I_2) = \int_{-\frac{h}{2}}^{\frac{h}{2}} ((1, (z - e)^2) \rho(z)) dz \quad (67)$$

For free vibration analysis, the work done by external forces (W) are neglected. The Hamilton's principal Eq. (64) leads to the following dynamic equilibrium equation of a system [13, 51]:

$$[K_e]\{q_e\} + [M^e]\{\ddot{q}_e\} = 0 \quad (68)$$

$$([K_e] - \omega^2[M^e])\{q_e\} = 0 \quad (69)$$

where ω indicates the fundamental frequency, and $[M^e]$ represents the mass matrix written as:

$$[M^e] = \int_{\Omega} [N]^T [I] [N] d\Omega \quad (70)$$

$[I]$ represents the inertia matrix presented by:

$$[I] = \begin{bmatrix} I_0 & 0 & 0 & 0 & 0 & 0 \\ 0 & I_0 & 0 & 0 & 0 & 0 \\ 0 & 0 & 0 & 0 & 0 & 0 \\ 0 & 0 & 0 & I_0 & 0 & 0 \\ 0 & 0 & 0 & 0 & I_2 & 0 \\ 0 & 0 & 0 & 0 & 0 & I_2 \end{bmatrix} \quad (71)$$

3.3.3 Mechanical buckling

The external work of in-plane forces due to mechanical loading can be given by [11, 13]:

$$W = \int_{\Omega} \left\{ \varepsilon^{nl} \right\}^T [N] d\Omega \quad (72)$$

Using Eqs. (52), (57), and (72), the total potential energy may be formulated as:

$$\pi = \left[\frac{1}{2} \int_{\Omega} \left(\{q_e\}^T \left([B_m]^T [D_m] [B_m] + [B_b]^T [D_b] [B_b] + [B_s]^T [D_s] [B_s] \right) \{q_e\} \right) d\Omega \right] - \left[\frac{1}{2} \int_{\Omega} \{q_e\}^T [B_g]^T [\bar{N}] [B_g] \{q_e\} d\Omega \right] \quad (73)$$

where $[\bar{N}] = \begin{bmatrix} N_x & N_{xy} \\ N_{xy} & N_y \end{bmatrix}$ is the stress matrix caused by mechanical loading.

The following eigenvalue problem is obtained by canceling the second potential energy variation ($\pi = 0$) with respect to the nodal values $\{q_e\}$ [13]:

$$\left([K_e] + [K_g^e] \right) \{q_e\} = 0 \quad (74)$$

where $[K_g^e]$ represent the geometric elementary matrix given by [52]:

$$[K_g^e] = \int_{\Omega} [B_g]^T [\bar{N}] [B_g] d\Omega \quad (75)$$

Introducing the loading factor λ , the stress matrix can be written as $[\bar{N}] = \lambda [\bar{N}_0]$; then, the geometric elementary matrix can be expressed as:

$$[K_{g0}^e] = \int_{\Omega} [B_g]^T [\bar{N}_0] [B_g] d\Omega \quad (76)$$

where $[\bar{N}_0]$ is the stress matrix resulting from applied mechanical load N_0 .

The eigenvalue problem used to evaluate the buckling critical load can be given by [12, 13]:

$$\det \left([K_e] + \lambda [K_{g0}^e] \right) = 0 \quad (77)$$

Finally, the critical buckling load is given by:

$$N_{cr} = \lambda_{cr} N_0 \quad (78)$$

After determining the structural stiffness $[K]$, mass $[M]$, and geometrical $[K_g]$ matrices for all elements, and also the structural load vector $\{F\}$ by assembling the element stiffness $[K^e]$, mass $[M^e]$, and $[K_{g0}^e]$ matrices given in Eqs. (62), (70), (76), respectively, and equivalent nodal load $\{F_e\}$, the following equations can be applied to study static, free vibrational, and buckling analyses of the FGM plate, respectively [52]:

$$[K] \{q_e\} = \{F\} \quad (79)$$

$$([K] - \omega^2 [M]) \{q_e\} = 0 \quad (80)$$

$$([K] - \lambda_{cr} [K_g]) \{q_e\} = 0 \quad (81)$$

Table 1 The characteristics of the materials used in FG plates

Properties	Metal		Ceramic		
	Aluminum* (Al*)	Aluminum (Al)	Zirconia (ZrO ₂ – 2)	Zirconia (ZrO ₂ – 1)	Alumina (Al ₂ O ₃)
E (Gpa)	70	70	200	151	380
ν	0.3	0.3	0.3	0.3	0.3
ρ (kg/m ³)	2702	2707	5700	3000	3800

Table 2 Boundary conditions of plates

Boundary conditions	Abbreviations	Restrained edges
Simply supported	SSSS	at $x = 0, l: v = w = \beta_y = 0$ at $y = 0, L: u = w = \beta_x = 0$
Clamped	CCCC	at $x = 0, l; y = 0, L: u = v = w = \beta_x = \beta_y = \theta_z = 0$
Simply supported-clamped	SCSC	at $x = 0, l: u = v = w = \beta_x = \beta_y = \theta_z = 0$ at $y = 0, L: u = w = \beta_x = 0$
Simply supported-free	SFSF	at $y = 0, L: u = w = \beta_x = 0$
Simply-free-simply-clamped	SFSC	at $x = 0: u = v = w = \beta_x = \beta_y = \theta_z = 0$ at $y = 0, L: u = w = \beta_x = 0$
Simply supported-free	SFSS	at $x = 0: v = w = \beta_y = 0$ at $y = 0, L: u = w = \beta_x = 0$
Simply supported-clamped	SSSC	at $x = 0: u = v = w = \beta_x = \beta_y = \theta_z = 0$ at $x = l: v = w = \beta_y = 0$ at $y = 0, L: u = w = \beta_x = 0$

4 Results and discussions

In this paper, different numerical examples are investigated and analyzed to eluate the convergence, efficiency, and stability of the current element (SBRMP24) for static, dynamic, and buckling behaviors of FG rectangular plates. The results of current element are compared with previously presented results in the literature. Different FG plates have been studied, and their mechanical characteristics are shown in Table 1. For simplicity, the following non-dimensional expressions are used [11, 13]:

$$\bar{w} = \frac{10h^3 E_c}{L^4 q_0} w\left(\frac{L}{2}, \frac{l}{2}\right); \quad \bar{\sigma}_x = \frac{h}{q_0} \sigma_x\left(\frac{L}{2}, \frac{l}{2}, \frac{h}{2}\right); \quad \sigma_y = \frac{h}{q_0} \sigma_y\left(\frac{L}{2}, \frac{l}{2}, \bar{\tau} = \frac{h}{q_0} \tau_{xy}\right)\left(0, 0, -\frac{h}{3}\right) \quad (82)$$

$$\bar{w} = 100 E_m \left(\frac{h^3}{l^4}\right) \frac{w_c}{12q_0(1 - \vartheta^2)} \quad (83)$$

$$\bar{\beta} = \omega h \sqrt{\frac{\rho_m}{E_m}}; \quad \bar{\omega} = \omega \frac{l^2}{h} \sqrt{\frac{\rho_c}{E_c}} \quad (84)$$

$$\bar{\lambda}_{cr} = \lambda_{cr} \frac{(L^2)}{(E_m h^3)} \quad (85)$$

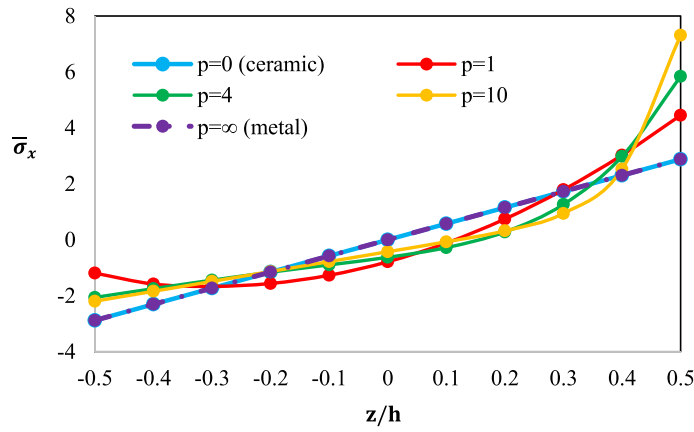
Various boundary conditions were considered in this paper are listed in Table 2.

4.1 Example 1: static analysis of FG plate under uniformly distributed loading (UDL)

In this example problem, we investigate a simply supported (SSSS), moderately thick square plate composed of aluminum (Al) and alumina (Al₂O₃) functionally graded (FG) material, with a side-to-thickness ratio ($l/h = 10$). The FG plate features a ceramic-rich Alumina top surface and a pure Aluminum bottom surface. Material properties for Aluminum and Alumina are detailed in Table 1. The distributed transverse load $q(x,y)$ is applied uniformly on the top surface ($z = h/2$) of the plate as a uniformly distributed load (UDL), denoted as $q(x, y) = q_0$. The objective of this example is to examine the influence of the gradient index on the bending behavior of FG plates. Table 3 presents the dimensionless deflection (\bar{w}) and stresses ($\bar{\sigma}_x, \bar{\sigma}_y, \bar{\tau}_{xy}$) obtained using varying mesh sizes: $8 \times 8, 12 \times 12, 16 \times 16$, and 20×20 , across different gradient index values (p). The numerical results of the current element are also compared and they are found to be in good agreement with

Table 3 Variation of the dimensionless deflection (\bar{w}) and stresses of FG plate for different gradient index (p) with ($L = l = 10 h$)

p	Mesh size	SBRMP 24				TSDT [2]	SSDT [3]	HSDT [11]
		8 × 8	12 × 12	16 × 16	20 × 20			
0 (ceramic)	\bar{w}	0.4657	0.4662	0.4664	0.4665	0.4665	0.4665	0.4663
	$\bar{\sigma}_x$	2.9163	2.8923	2.8839	2.8800	2.8920	2.8932	2.8656
	$\bar{\sigma}_y$	1.9442	1.9282	1.9226	1.9200	1.9106	1.9103	1.904
	$\bar{\tau}_{xy}$	1.2788	1.2902	1.2944	1.2963	1.2855	1.2850	1.266
1	\bar{w}	0.9270	0.9280	0.9284	0.9285	0.9421	0.9287	0.9282
	$\bar{\sigma}_x$	4.5075	4.4703	4.4573	4.4513	4.2598	4.4745	4.415
	$\bar{\sigma}_y$	2.2095	2.1912	2.1848	2.1819	2.2569	2.1692	2.164
	$\bar{\tau}_{xy}$	1.1040	1.1140	1.1176	1.1194	1.1572	1.1143	1.093
2	\bar{w}	1.1886	1.1899	1.1903	1.1906	1.2227	1.1940	1.1948
	$\bar{\sigma}_x$	5.2631	5.2197	5.2045	5.1975	4.8881	5.2296	5.155
	$\bar{\sigma}_y$	2.0748	2.0577	2.0517	2.0490	2.1663	2.0338	2.032
	$\bar{\tau}_{xy}$	0.9840	0.9928	0.9961	0.9976	1.0448	0.9907	0.9745
4	\bar{w}	1.3744	1.3758	1.3763	1.3765	—	1.3890	1.3916
	$\bar{\sigma}_x$	5.9189	5.8702	5.8531	5.8452	—	5.8915	5.797
	$\bar{\sigma}_y$	1.7598	1.7453	1.7402	1.7379	—	1.7197	1.724
	$\bar{\tau}_{xy}$	1.0265	1.0356	1.0390	1.0405	—	1.0298	1.016
10	\bar{w}	1.5668	1.5684	1.5689	1.5692	1.6054	1.5876	1.5934
	$\bar{\sigma}_x$	7.4053	7.3445	7.3232	7.3134	6.9539	7.3689	7.253
	$\bar{\sigma}_y$	1.3145	1.3038	1.3000	1.2982	1.3349	1.2820	1.288
	$\bar{\tau}_{xy}$	1.0687	1.0781	1.0815	1.0831	1.1119	1.0694	1.058
∞ (metal)	\bar{w}	2.4996	2.5049	2.5104	2.5221	—	2.5327	—
	$\bar{\sigma}_x$	2.9163	2.8923	2.8839	2.8800	—	2.8932	—
	$\bar{\sigma}_y$	1.9442	1.9282	1.9226	1.9200	—	1.9103	—
	$\bar{\tau}_{xy}$	1.2788	1.2902	1.2944	1.2963	—	1.2850	—

**Fig. 4** Variations of dimensionless in-plane stress ($\bar{\sigma}_x$) for a square FGM plate subjected to UDL with various gradient index (p)

the analytical solution of Zenkour [3] using second-order shear deformation theory (SSDT), Reddy [2] using TSDT, and numerical results based on HSDT presented by Tati [11]. As illustrated in Table 3, it is evident to observe that the dimensionless stresses on a metal plate ($p = \infty$) are identical to those on a ceramic plate ($p = 0$). This is because in both cases the plate is completely homogeneous. The stresses remain independent of the modulus of elasticity. It can also be observed that the dimensionless deflection (\bar{w}) and normal stress ($\bar{\sigma}_x$) increase as the gradient index (p) increases, while $\bar{\sigma}_y$ decreases. The in-plane shear stress $\bar{\tau}_{xy}$ decreases in the range of (p) from 0 to 2, then increases with increasing gradient index. For a better illustration, Figs. 4 and 5 show, respectively, the changes of the dimensionless normal stress ($\bar{\sigma}_x$), and in-plane shear stress ($\bar{\tau}_{xy}$) across the thickness with five gradient index (p). It can be seen that the distribution of in-plane normal and shear stresses through the thickness is nearly linear for isotropic plates ($p = 0$ (ceramic) and $p = \infty$ (metal)), and becomes non-linear for graded plates when $p = 1, 2, 5$, and 10.

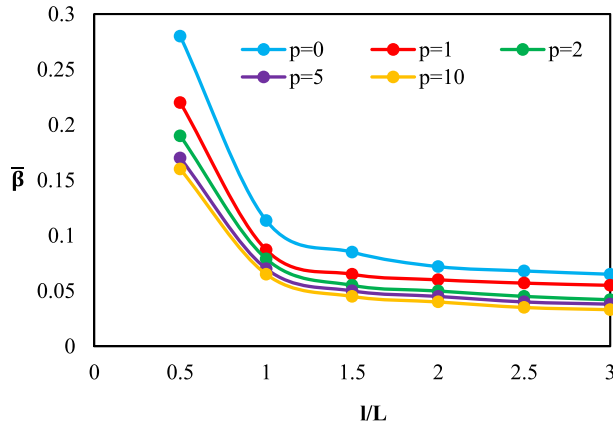


Fig. 5 Variations of dimensionless in-plane shear stress ($\bar{\beta}_{xy}$) for a square FGM plate subjected to UDL with various gradient index (p)

Table 4 Dimensionless deflection (\bar{w}) of Al/ZrO₂-2 FG plate with ($L = l = 5$ h)

BC	Methods	p				
			0	0.5	1	2
SSSS	SBRMP24 (8 × 8)	0.1713	0.2320	0.2715	0.3111	
	SBRMP24 (12 × 12)	0.1715	0.2322	0.2717	0.3113	
	SBRMP24 (16 × 16)	0.1717	0.2324	0.2719	0.3115	
	SBRMP24 (20 × 20)	0.1717	0.2324	0.2719	0.3115	
	SBQP20 (20 × 20) [14]	0.1714	0.2321	0.2716	0.3111	
	IGA-Quadratic [53]	0.1717	0.2324	0.2719	0.3115	
	MITC4 [7]	0.1715	0.2317	0.2704	0.3093	
	NS-DSG3 [7]	0.1721	0.2326	0.2716	0.3107	
CCCC	SBRMP24 (8 × 8)	0.0755	0.1006	0.1174	0.1359	
	SBRMP24 (12 × 12)	0.0758	0.1010	0.1179	0.1365	
	SBRMP24 (16 × 16)	0.0759	0.1011	0.1181	0.1367	
	SBRMP24 (20 × 20)	0.0759	0.1012	0.1181	0.1368	
	SBQP20 (20 × 20) [14]	0.0759	0.1011	0.1180	0.1366	
	IGA-Quadratic [53]	0.0760	0.1013	0.1183	0.1369	
	MITC4 [7]	0.0758	0.1010	0.1179	0.1365	
	NS-DSG3 [7]	0.0788	0.1051	0.1227	0.1420	

Next, the bending behavior of the FG thick square plate has also been examined for a uniformly distributed load (UDL). The plate is made of aluminum (Al) and zirconia (ZrO₂-2) and their corresponding material characteristics are listed in Table 1. The obtained results of the dimensionless deflection (\bar{w}) are presented in Table 4 for various gradient index (p) and two boundary conditions, simply supported (SSSS) and clamped (CCCC) with side-to-thickness ratio $l/h = 5$ using several meshes sizes: 8 × 8, 12 × 12, 16 × 16, and 20 × 20. A comparison is made between the results obtained from the proposed element and those found in the literature [7, 14, 53], revealing excellent agreement. It can also be noticed that the results of the current element SBRMP24 converge very quickly for all meshes.

4.2 Example 2: free vibration analysis of FG plate

In the second example, the current finite element formulation has been employed to analyze the natural vibration behaviors of different FG plates. Furthermore, we investigated the impact of specific parameters on the vibrational characteristics of these plates. In the first instance, the convergence of the present element SBRMP24 is checked for the free vibrational behavior of SSSS (Al*/ZrO₂-2) square plate. The dimensionless natural frequencies ($\bar{\beta}$) of FG plate are summarized in Table 5 for various side-to-thickness ratios (l/h) and gradient indexes (p), using four meshes (8 × 8, 12 × 12, 16 × 16, and 20 × 20) and compared with (3D) precise model of Vel and Batra [5], an analytical results of Thai et al. [54] using simple FSDT, (2D) HSDT solutions of Matsunaga [6], a non-polynomial HSDT proposed by Mantari et al. [8], and a new trigonometric shear

Table 5 Dimensionless natural frequencies ($\bar{\beta}$) of Al*/ZrO₂-2 square plates

Theory	$p = 0^*$		$p = 1$			$l/h = 5$		
	$l/h = \sqrt{10}$	$l/h = 10$	$l/h = 5$	$l/h = 10$	$l/h = 20$	$p = 2$	$p = 3$	$p = 5$
SBRMP24 (8 × 8)	0.4596	0.0571	0.2260	0.0613	0.0157	0.2247	0.2260	0.2275
SBRMP24 (12 × 12)	0.4608	0.0574	0.2269	0.0616	0.0158	0.2256	0.2269	0.2283
SBRMP24 (16 × 16)	0.4612	0.0575	0.2272	0.0617	0.0158	0.2259	0.2272	0.2286
SBRMP24 (20 × 20)	0.4614	0.0576	0.2273	0.0617	0.0158	0.2261	0.2273	0.2288
3D [5]	0.4658	0.0578	0.2192	0.0596	0.0153	0.2197	0.2211	0.2225
S-FSDT [54]	0.4618	0.0577	0.2173	0.0592	0.0152	0.2189	0.2207	0.2222
(2D) HSDT [6]	0.4658	0.0578	0.2285	0.0619	0.0158	0.2264	0.2270	0.2281
HSDT[8]	0.4624	0.0577	0.2277	0.0619	0.0158	0.2257	0.2263	0.2271
TSDT [13]	0.4625	0.0578	0.2280	0.0620	0.0159	0.2253	0.2254	0.2258

$$\bar{\beta}^* = \omega h \sqrt{\frac{\rho_c}{E_c}}$$

Table 6 Dimensionless natural frequencies ($\bar{\beta}$) of Al*/Al₂O₃ square plates

Theory		l/L	l/h	p	3D [55]	HSDT [8]	TSDT [13]	SBRMP24
1	10	0	0	0.1135	0.1134	0.1136	0.1132	
			1	0.0870	0.0868	0.0870	0.0866	
			2	0.0789	0.0788	0.0788	0.0787	
			5	0.0741	0.0740	0.0738	0.0748	
		5	0	0.4169	0.4151	0.4156	0.4144	
			1	0.3222	0.3205	0.3210	0.3200	
			2	0.2905	0.2892	0.2883	0.2901	
			5	0.2676	0.2666	0.2632	0.2708	
	2	0	0	1.8470	1.8277	1.8224	1.8197	
			1	1.4687	1.4460	1.4435	1.4411	
			2	1.3095	1.2896	1.2675	1.3003	
			5	1.1450	1.1312	1.0829	1.1786	
2	10	0	0	0.0719	0.0717	0.0722	0.0716	
			1	0.0550	0.0549	0.0553	0.0548	
			2	0.0499	0.0498	0.0501	0.0498	
			5	0.0471	0.0470	0.0472	0.0538	
		5	0	0.2713	0.2705	0.2721	0.2700	
			1	0.2088	0.2081	0.2094	0.2077	
			2	0.1888	0.1882	0.1888	0.1885	
			5	0.1754	0.1750	0.1743	0.1768	
	2	0	0	0.9570	1.2910	1.2943	0.9569	
			1	0.7937	1.0137	1.0172	0.7961	
			2	0.7149	0.9067	0.8988	0.7193	
			5	0.6168	0.8064	0.7824	0.6214	

deformation theory (TSDT) proposed by Sadgui and Tati [13]. There is excellent agreement between the above references. But they are more similar to HSDT solutions.

In this example, we also investigated the influence of some parameters like the gradient index (p), side-to-thickness ratios (l/h), and aspect ratios (L/L) on the dimensionless natural frequencies ($\bar{\beta}$). The results are presented in Table 6 using a mesh size with 20 × 20 elements and also plotted in Fig. 6 for illustration purposes. Table 6 presents the dimensionless natural frequencies ($\bar{\beta}$) of a simply supported FGM plate made of aluminum (Al*) and alumina (Al₂O₃) for different gradient index (p) and side-to-thickness ratios (l/h). Both square ($L = 1$) and rectangular ($l = 2L$) plates are considered. The obtained results are compared with the (3D) vibration method developed by Jin et al. [55], a non-polynomial HSDT proposed by Mantari et al. [8], and TSDT presented by Sadgui and Tati [13]. It can be seen from Table 6 that the current results are in good agreement with the mentioned references, from the thin to the thick plates. However, they are more similar to those presented by Mantari et al. [8]. It can be also seen that the dimensionless natural frequencies ($\bar{\beta}$) reduce as the gradient index (p), and aspect ratio (L/L) increase, as shown in Fig. 6.

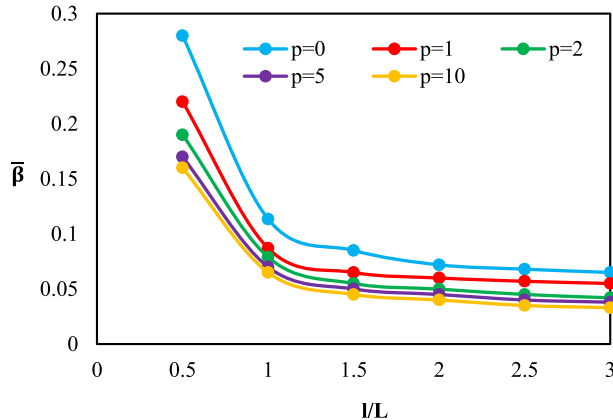


Fig. 6 Influence of aspect ratios (l/L) on dimensionless natural frequencies ($\bar{\beta}$) of $\text{Al}^*/\text{Al}_2\text{O}_3$ rectangular plates ($l/h = 10$).

Table 7 Dimensionless deflection (\bar{w}) of FG square plates for different boundary conditions

l/h	p	Boundary conditions						
		CCCC	SCSC	SSSC	SSSS	SFSC	SFSS	SFSF
5	0	0.2369	0.3296	0.4178	0.5356	0.8045	1.0196	1.6531
	1	0.4451	0.6247	0.8035	1.0452	1.5652	2.0056	3.2649
	2	0.5731	0.8038	1.0327	1.3420	2.0102	2.5737	4.1885
	5	0.7283	1.0115	1.2791	1.6359	2.4587	3.1102	5.0392
	10	0.7938	1.0879	1.3481	1.6887	2.5477	3.1718	5.1067
	0	0.1641	0.2406	0.3336	0.4665	0.6847	0.9248	1.5310
10	1	0.3211	0.4728	0.6601	0.9285	1.3602	1.8452	3.0628
	2	0.4122	0.6068	0.8467	1.1906	1.7443	2.3655	3.9261
	5	0.5009	0.7341	1.0168	1.4201	2.0852	2.8142	4.6644
	10	0.5610	0.8118	1.1291	1.5692	2.3078	3.1036	5.1388
	0	0.1447	0.2169	0.3114	0.4492	0.6521	0.8987	1.5022
	1	0.2882	0.4326	0.6223	0.8994	1.3046	1.8042	3.0106
20	2	0.3696	0.5546	0.7977	1.1527	1.6723	2.3123	3.8584
	5	0.4405	0.6601	0.9473	1.3662	1.9834	2.7387	4.5681
	10	0.4865	0.7282	1.0433	1.5024	2.1825	3.0102	5.0196
	0	0.1391	0.2100	0.3050	0.4443	0.6424	0.8935	1.4934
	1	0.2786	0.4210	0.6115	0.8912	1.2882	1.7922	2.9955
	2	0.3571	0.5395	0.7836	1.1421	1.6508	2.2968	3.8388
50	5	0.4229	0.6387	0.9273	1.3510	1.9532	2.7167	4.5404
	10	0.4648	0.7018	1.0186	1.4837	2.1452	2.9832	4.9856
	0	0.1382	0.2090	0.3040	0.4437	0.6409	0.8925	1.4902
	1	0.2771	0.4192	0.6098	0.8900	1.2856	1.7905	2.9896
	2	0.3552	0.5372	0.7815	1.1406	1.6475	2.2945	3.8312
	5	0.4202	0.6355	0.9243	1.3489	1.9485	2.7135	4.5306
100	10	0.4614	0.6978	1.0149	1.4809	2.1394	2.9791	4.9741

4.3 Example 3: Static and free vibration analysis of FG plate under different boundary conditions

The next example is performed for thin and thick SSSS $\text{Al}^*/\text{Al}_2\text{O}_3$ square plates. Tables 7 and 8 present the dimensionless deflection (\bar{w}) and dimensionless natural frequencies ($\bar{\omega}$) of $\text{Al}^*/\text{Al}_2\text{O}_3$ square plates subjected to uniform loads. The side-to-thickness ratio varies from 5 to 100, with corresponding l/h values of 5 (representing thick plates), 10, 20 (moderately thick plates), 50, and 100 (indicating thin plates), while considering five different power law index values. Additionally, seven combinations of boundary conditions are examined. This example aims to assess the impact of the side-to-thickness ratio, gradient index, and boundary conditions on both the static and free vibrational behavior of FG plates. For a more illustrative example, parts of Tables 7 and 8 are also presented in Figs. 7, 8, 9, and 10.

Figure 7 shows the variation of the dimensionless deflection (\bar{w}) of a square FG plate versus the side-to-thickness ratio l/h with different boundary conditions and ($p = 1$). The plate is subjected to (UDL). As can be seen, the dimensionless deflection decreases by increasing the l/h ratio. After $l/h = 10$, it is observed that the

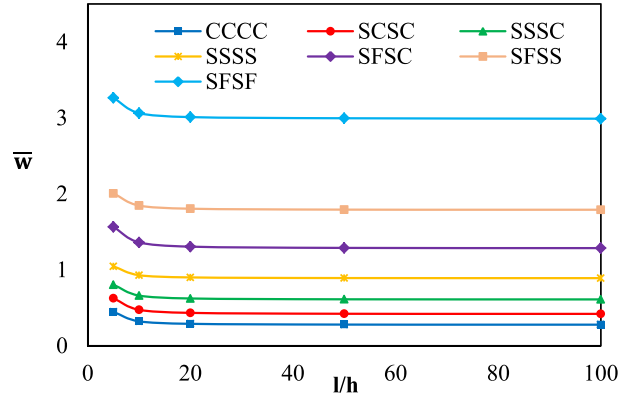


Fig. 7 The influence of side/thickness ratios (l/h) on dimensionless deflection (\bar{w}) of square plates exposed to boundary conditions ($p = 1$)

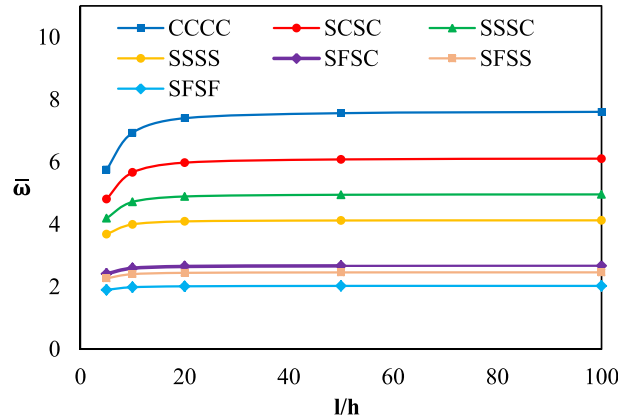


Fig. 8 The influence of side/thickness ratios (l/h) on dimensionless natural frequencies ($\bar{\omega}$) of square plates exposed to boundary conditions ($p = 2$)

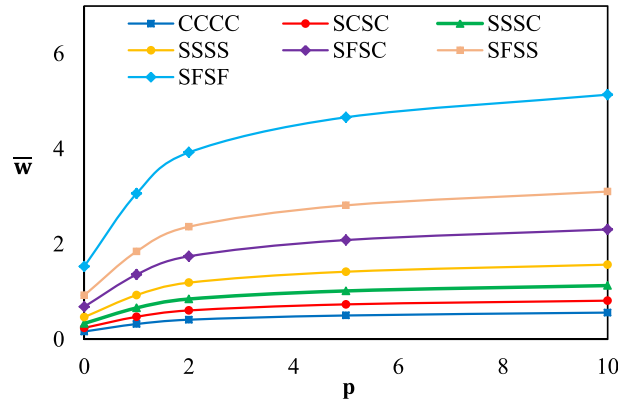
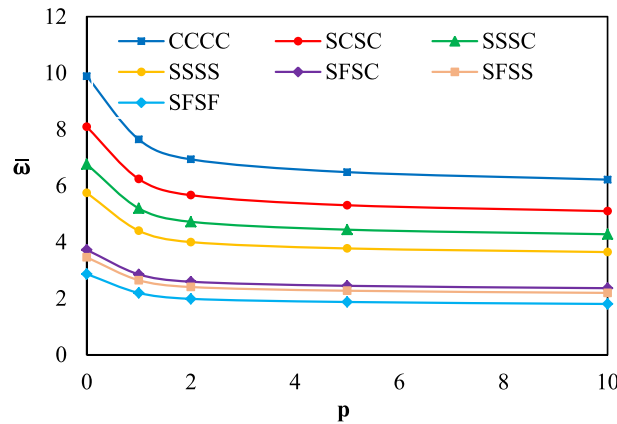


Fig. 9 The influence of gradient index (p) on dimensionless deflection (\bar{w}) of square plates exposed to boundary conditions ($l/h = 10$)

Table 8 Dimensionless natural frequencies ($\bar{\omega}$) of FG square plates for different boundary conditions

l/h	p	Boundary conditions						
		CCCC	SCSC	SSSC	SSSS	SFSC	SFSS	SFSF
5	0	8.0644	6.7759	5.9548	5.2637	3.4524	3.2503	2.7238
	1	6.3544	5.3127	4.6297	4.0643	2.6618	2.5004	2.0930
	2	5.7554	4.8118	4.1946	3.6838	2.4141	2.2682	1.8996
	5	5.2616	4.4202	3.8876	3.4393	2.2587	2.1276	1.7542
	10	5.1168	4.3295	3.8525	3.4420	2.2671	2.14262	1.6824
	0	9.8854	8.0891	6.7633	5.7466	3.7236	3.4563	2.8652
	1	7.6392	6.2372	5.1946	4.4015	2.8520	2.6447	2.1935
	2	6.9349	5.6631	4.7177	3.9982	2.5913	2.4032	1.9832
	5	6.4813	5.3055	4.4385	3.7732	2.4462	2.2711	1.8721
	10	6.2148	5.0962	4.2767	3.6438	2.3624	2.1950	1.8023
20	0	10.629	8.5901	7.0388	5.8949	3.8132	3.5205	2.9006
	1	8.1439	6.5760	5.3819	4.5036	2.9137	2.6891	2.2188
	2	7.4016	5.9770	4.8922	4.0940	2.6488	2.4448	2.0126
	5	6.9880	5.6481	4.6291	3.8774	2.5085	2.3161	1.9065
	10	6.7468	5.4567	4.4767	3.7523	2.4273	2.2417	1.8423
	0	10.887	8.7553	7.1252	5.9391	3.8426	3.5408	2.9180
	1	8.3167	6.6867	5.4403	4.5339	2.9336	2.7030	2.2254
	2	7.5619	6.0799	4.9467	4.1226	2.6675	2.4579	2.0254
	5	7.1645	5.7617	4.6891	3.9087	2.5290	2.3304	1.9201
	10	6.9342	5.5773	4.5400	3.7849	2.4488	2.2566	1.8593
50	0	10.949	8.7914	7.1419	5.9457	3.8479	3.5440	2.9202
	1	8.3636	6.7134	5.4525	4.5385	2.9374	2.7052	2.2284
	2	7.6048	6.1044	4.9580	4.1269	2.6710	2.4599	2.0258
	5	7.2062	5.7860	4.7006	3.9134	2.5326	2.3326	1.9201
	10	6.9758	5.6018	4.5517	3.7898	2.4526	2.2590	1.8612

**Fig. 10** The influence of gradient index (p) on dimensionless natural frequencies ($\bar{\omega}$) of square plates exposed to boundary conditions ($l/h = 10$)

dimensionless deflection curves follow a parallel line pattern. It can be also seen from this figure that as the boundary constraints increase, the dimensionless deflection decreases.

Figure 8 depicts the variation of the dimensionless natural frequencies ($\bar{\omega}$) versus the side-to-thickness ratio l/h for square FG plate with different boundary conditions. From this figure, it can be observed that with a particular gradient index ($p = 2$), the dimensionless natural frequencies increase with the increase in the side-to-thickness ratio up to $a/h = 20$ and then vary constantly in all cases. This probably can be explained by the effect of shear deformation which is less significant when the thickness decreases ($a/h > 20$) as indicated by [13, 51]. To conclude, the dimensionless natural frequencies of thick FG plates are more sensitive to changes in the side-to-thickness ratio compared to thin ones. It can be also observed from Fig. 8 that the dimensionless frequency increases with the increasing constraints at the edges of plates. This behavior is due to the fact that higher constraints at the edges increase the bending stiffness of the plate, resulting in higher vibrational responses.

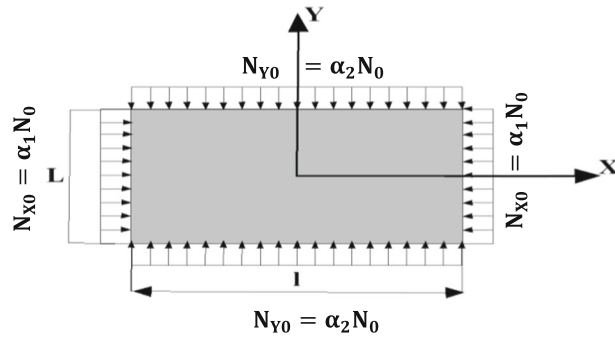


Fig. 11 FG rectangular plate under in-plane loading

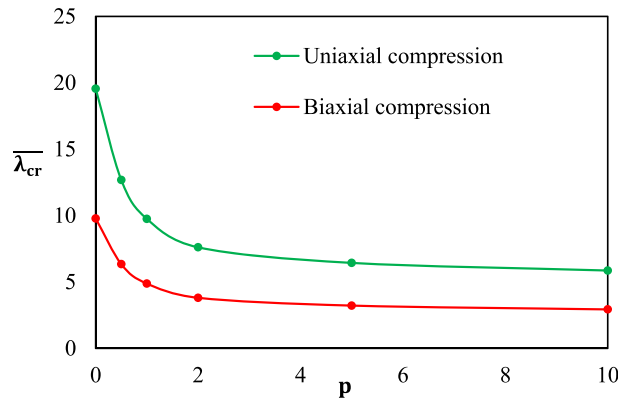


Fig. 12 The influence of gradient index p on dimensionless critical buckling load ($\bar{\lambda}_{cr}$) of Al/Al₂O₃ square plate ($l/h = 100$) with various types of loading

Figure 9 illustrates the effect of gradient index p on the dimensionless deflection (\bar{w}) of square plates ($l/h = 10$) with different boundary conditions. It is observed from the figure that increasing the gradient index results in an increase in the dimensionless deflection. This is due to the fact that increasing the gradient index increases the volume fraction of metal which reduces the FG plate bending stiffness and makes these FG plates more flexible, resulting in higher deflection. It can be also noticed from Fig. 9 that the deflection is maximum for the simply supported free boundary condition and it is minimum for all sides clamped condition. This behavior is because higher constraints at the edges of plates increase the bending stiffness of the plate, resulting in lower bending responses.

Figure 10 shows the variation of the dimensionless natural frequencies ($\bar{\omega}$) of square plates ($l/h = 10$) with different boundary conditions. It can be observed that the dimensionless natural frequencies decrease by increasing the gradient index p . This is because the increase in the gradient index decreases the volume fraction of the ceramic and, consequently, the plate bending stiffness. It can be also seen from this figure that as the boundary constraints increase, the dimensionless natural frequencies increase.

In the last example, the validity of the current element (SBRP24) is also tested for buckling analysis of SSSS Al/Al₂O₃ rectangular plates exposed to uniaxial ($\alpha_1 = 1, \alpha_2 = 0$) and biaxial ($\alpha_1 = 1, \alpha_2 = 1$) compression loads as shown in Fig. 11, with ($l/L = 1, 2$ and $l/h = 100$). The dimensionless critical buckling load ($\bar{\lambda}_{cr}$) load of FG plate is presented in Tables 9 and 10 using various meshes and five gradient index (p) values. This example aims to examine the influence of aspect ratios (l/L), and gradient index (p), on the buckling analysis of the FG plate. The comparison of the current results with the analytical results of Reddy [56] based on HSDT, Levy solution of Thai and Choi [57] based on refined plate theory, Zenkour and Aljadani [58] using refined HSDT, and the numerical results of Sadgui and Tati [13] using TSDT theory and Belounar et al. [15] using FSDT. The results found for the current element (SBRMP24) are in excellent agreement with the results mentioned in the above references. In addition, they are more similar to those obtained by Belounar et al. [15]. It should be concluded from the above tables and Fig. 12 that the dimensionless critical buckling load ($\bar{\lambda}_{cr}$) of the plate exposed to uniaxial loading is bigger than that exposed to biaxial loading. Moreover, for rectangular plates ($l/L = 2$), these values are higher compared to square plates ($l/L = 1$).

Table 9 Dimensionless critical buckling load ($\bar{\lambda}_{\text{cr}}$) of Al/Al₂O₃ square plate ($l/L = 1$)

(α_1, α_2)	Theory	Gradient index p				
		$p = 0$	$p = 1$	$p = 2$	$p = 5$	$p = 10$
(1, 0)	SBRMP24 (8 × 8)	19.2601	9.6024	7.4930	6.3347	5.7692
	SBRMP24 (12 × 12)	19.4479	9.6945	7.5649	6.3966	5.8261
	SBRMP24 (16 × 16)	19.5198	9.7302	7.5928	6.4203	5.8477
	SBRMP24 (20 × 20)	19.5537	9.7472	7.6060	6.4315	5.8579
	Belouar et al. [15]	19.5534	9.7471	7.6058	6.4314	5.8576
	Sadgui and Tati [13]	19.6812	9.8107	7.6551	6.4724	5.8949
	Reddy [56]	19.5700	9.7500	7.6100	6.4300	5.8600
	Zenkour and Aljadani [58]	19.6145	9.7775	7.6293	6.4507	5.8752
	Thai and Choi [57]	19.6145	9.7775	7.6293	6.4507	5.8752
	SBRMP24 (8 × 8)	9.6300	4.8012	9.5374	3.1674	2.8846
	SBRMP24 (12 × 12)	9.7239	4.8472	3.7825	3.1983	2.9131
	SBRMP24 (16 × 16)	9.7599	4.8651	3.7964	3.2101	2.9239
(1, 1)	SBRMP24 (20 × 20)	9.7769	4.8736	3.8031	3.2158	2.9291
	Belouar et al. [15]	9.7767	4.8735	3.8029	3.2157	2.9288
	Sadgui and Tati [13]	9.8406	4.9053	3.8275	3.2362	2.9474
	Reddy [56]	9.7880	4.8790	3.8070	3.2190	2.9320
	Zenkour and Aljadani [58]	9.8072	4.8887	3.8146	3.2253	2.9375
	Thai and Choi [57]	9.8073	4.8888	3.8147	3.2254	2.9376

Table 10 Dimensionless critical buckling load ($\bar{\lambda}_{\text{cr}}$) of Al/Al₂O₃ square plate ($l/L = 2$)

(α_1, α_2)	Theory	Gradient index p				
		$p = 0$	$p = 1$	$p = 2$	$p = 5$	$p = 10$
(1, 0)	SBRMP24 (16 × 8)	76.8584	38.3241	29.9050	25.2783	23.0176
	SBRMP24 (24 × 12)	77.6567	38.7207	30.2146	25.5410	23.2572
	SBRMP24 (32 × 16)	77.9468	38.8654	30.3275	25.6364	23.3441
	Belouar et al. [15]	78.0780	38.9208	30.3704	25.6808	23.3898
	Sadgui and Tati [13]	78.7471	39.2647	30.6328	25.8836	23.5667
	Reddy [56]	77.7100	38.7400	30.2200	25.5400	23.2600
	Zenkour and Aljadani [58]	78.3256	39.0545	30.4707	25.7491	23.4455
	Thai and Choi [57]	78.3257	39.0546	30.4707	25.7491	23.4456
	SBRMP24 (16 × 8)	24.4534	12.1914	9.5133	8.0428	7.3244
	SBRMP24 (24 × 12)	24.4763	12.2026	9.5221	8.0504	7.3313
	SBRMP24 (32 × 16)	24.4854	12.2071	9.5256	8.0533	7.3340
	Belouar et al. [15]	24.5111	12.2180	9.5339	8.0621	7.3430
(1, 1)	Sadgui and Tati [13]	24.6209	12.2748	9.5770	8.0948	7.3714
	Reddy [56]	24.3780	12.5820	9.482	8.0150	7.299
	Zenkour and Aljadani [58]	24.4974	12.2132	9.5293	8.0549	7.3353
	Thai and Choi [57]	24.4974	12.2132	9.5294	8.0550	7.3353

Figures 13 and 14 illustrate variations of dimensionless critical buckling load ($\bar{\lambda}_{\text{cr}}$) exposed to uniaxial compression ($l = L = 10$ h, $\alpha_1 = 1$, $\alpha_2 = 0$) versus gradient index (p) and modulus ratio (E_m/E_c), respectively. It should be noticed that the dimensionless critical buckling load ($\bar{\lambda}_{\text{cr}}$) reduces as the gradient index (p) and modulus ratio (E_m/E_c) increase.

Figure 15 shows the variation of dimensionless critical buckling load ($\bar{\lambda}_{\text{cr}}$) under uniaxial compression versus length-to-thickness ratio (l/h) for different gradient index p . It is observed that the dimensionless critical buckling load increases with increasing length-to-thickness ratio. In principle, a thinner FG plate has a higher critical buckling than a thicker FG plate.

Figure 16 displays dimensionless critical buckling load under biaxial compression versus length-to-width ratio (l/L) with $l/h = 100$ and various gradient index p . It is also remarked that the dimensionless critical buckling load increases as the aspect ratio (l/L) increases.

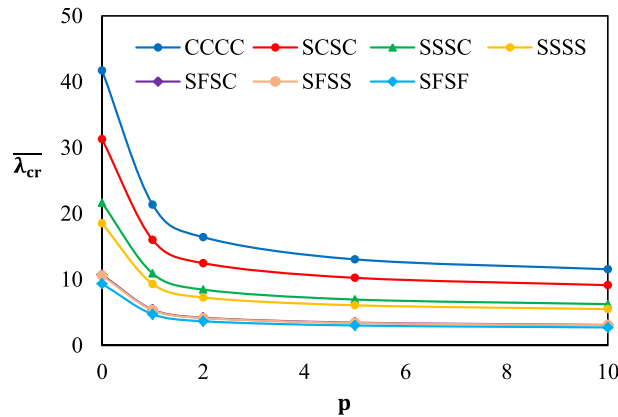


Fig. 13 Dimensionless critical buckling load ($\bar{\lambda}_{cr}$) of square plates versus p with various boundary conditions under uniaxial compression

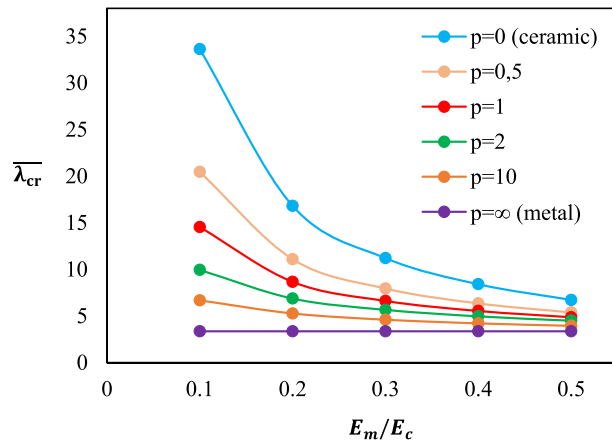


Fig. 14 Dimensionless critical buckling load ($\bar{\lambda}_{cr}$) of square plates versus E_m/E_c with various gradient index (p) under uniaxial compression

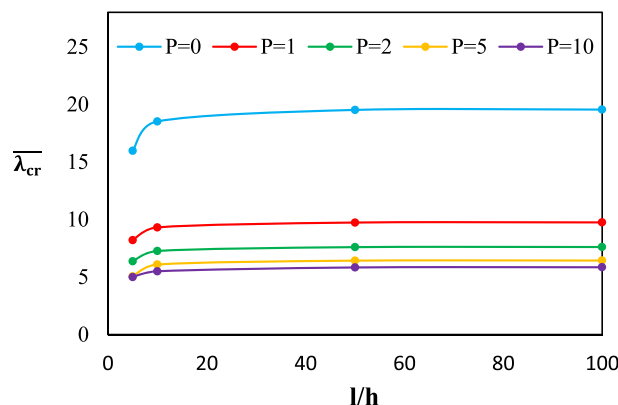


Fig. 15 Dimensionless critical buckling load ($\bar{\lambda}_{cr}$) of square plates versus side/ thickness ratios (l/h) with various gradient index (p) of the FGM under uniaxial compression

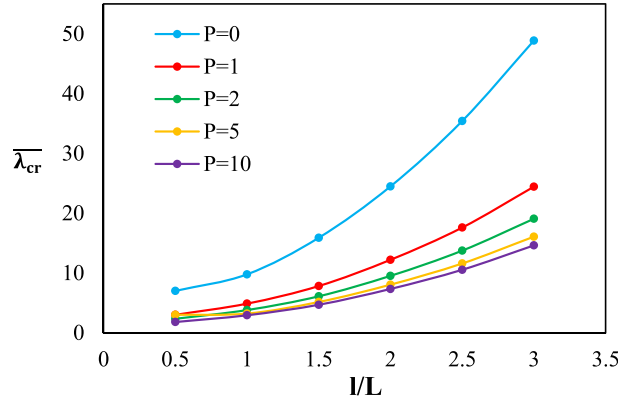


Fig. 16 Dimensionless critical buckling load ($\bar{\lambda}_{cr}$) of square plates versus aspect ratio (l/L) with various gradient index (p) of the FGM under biaxial compression

5 Conclusion

A complete study of the static, free vibrational, and buckling behaviors of rectangular and square FG plates is investigated using a 4-node rectangular plate element, which has six degrees of freedom at each node based on the strain approach and FSDT. The characteristics of the FG plate are considered to change through the thickness direction by the power law function. The notion of a neutral surface has been used to prevent the membrane-bending effect. The displacement functions of the current element, which have higher order expressions, based on assumed strain functions satisfying both rigid body modes and compatibility equations. The potential energy and the principle of Hamilton are applied to obtain the rigidity, mass, and geometrical matrices. Convergence and validation studies have been carried out to inculcate the accuracy of the present formulation. Furthermore, the impacts of several factors such as thickness ratios (l/h), gradient index (p), aspect ratios (l/L), and loading type with varying boundary conditions on the bending, free vibration and buckling behavior of FG plates are discussed and analyzed. Some of the impacts can be summarized as follows:

- The current element (SBRMP24) is efficient and accurate in predicting of the bending, free vibration and stability behaviors of FGM plates.
- The dimensionless deflection (\bar{w}) and in-plane normal stress ($\bar{\sigma}_x$) increase with increasing gradient index (p), while the in-plan stress ($\bar{\sigma}_y$) and shear stress ($\bar{\tau}_{xy}$) decreases.
- The stresses for a totally ceramic plate are the same as that for a totally metal plate. This is due to the fact that in both cases the plate is completely homogeneous.
- The dimensionless deflection decreases by increasing the (l/h) ratio whereas it increases with the increasing of gradient index values.
- Independent of boundary conditions and the gradient index (p), increasing the thickness ratio results in a reduction of deflection and an increase in frequency. This is due to the effects of shear deformation.
- Independent of the boundary condition and the side-to-thickness ratio, as the gradient index (p) increases, the stiffness of the FGM plates decreases, and consequently, leads to an increase in the dimensionless deflection and a reduction in the dimensionless natural frequencies. This is because a higher gradient index (p) corresponds to a greater fraction of metal relative to ceramic, which makes these FG plates more flexible.
- Independent of the gradient index (p) and thickness ratio, increasing restrictions at the boundaries of the plates produce an increase in dimensionless natural frequencies and a decrease in the dimensionless deflection. Such behavior is due to the fact that higher constraints at the edges increase the flexural rigidity of the plate leading to higher vibration responses and lower bending.
- The dimensionless critical buckling loads and natural frequencies increase as the side-to thickness ratio and the boundary constraints increase and they decrease as the gradient index (p) and aspect ratio (l/L) increase.
- The dimensionless critical buckling load reduces as the gradient index (p) and modulus ratio (E_m/E_c) increase.
- The dimensionless critical buckling load of plate under uniaxial compression loading is greater than that under biaxial compression.

The current finite element formulation is a promising numerical approach for the simulation and computation of FG plates. It will be expanded in future for analyzing FG plates under thermo-mechanical buckling analysis and also for analyzing the behavior of FG microscale and nanoscale structures.

Author contributions T.A: Conceptualization, Data curation, Formal analysis, Investigation, Methodology, Writing—original draft, Writing—review and editing. M.B: Project administration, Investigation, Methodology, Supervision, Writing—review and editing. M. C : Investigation, Methodology, Writing—review and editing. All authors seen the final draft of the manuscript and take responsibility for its content

Data availability No datasets were generated or analysed during the current study.

Declarations

Conflict of interest The authors state that they have no conflicts of interest related to this paper.

Appendix

The membrane strains $\{\varepsilon_m\}$ specified in Eq. (30) satisfy the compatibility conditions as follows [32, 33]:

$$\frac{\partial^2 \varepsilon_x}{\partial y^2} + \frac{\partial^2 \varepsilon_y}{\partial x^2} - \frac{\partial^2 \gamma_{xy}}{\partial x \partial y} = 0 \quad (1a)$$

The curvatures and shear strains (κ_x , κ_y , κ_{xy} , γ_{xz} , γ_{yz}) specified in Eqs. (31)–(32) are satisfied by the compatibility equations below [37–40]:

$$\begin{aligned} \frac{\partial^2 \kappa_x}{\partial y^2} + \frac{\partial^2 \kappa_y}{\partial x^2} &= \frac{\partial^2 \kappa_{xy}}{\partial x \partial y} \\ \frac{\partial^2 \gamma_{xz}}{\partial x \partial y} - \frac{\partial^2 \gamma_{yz}}{\partial x^2} + \frac{\partial \kappa_{xy}}{\partial x} &= 2 \frac{\partial \kappa_x}{\partial y} \\ \frac{\partial^2 \gamma_{yz}}{\partial x \partial y} - \frac{\partial^2 \gamma_{xz}}{\partial y^2} + \frac{\partial \kappa_{xy}}{\partial y} &= 2 \frac{\partial \kappa_y}{\partial x} \end{aligned} \quad (2a)$$

References

1. Koizumi, M.: The concept of FGM. *Ceram. Trans. Funct. Graded Mater.* **34**, 3–10 (1993)
2. Reddy, J.N.: Analysis of functionally graded plates. *Int. J. Numer. Methods Eng.* **47**(1–3), 663–684 (2000)
3. Zenkour, A.M.: Analytical solution for bending of cross-ply laminated plates under thermo-mechanical loading. *Compos. Struct.* **65**(3), 367–379 (2004). <https://doi.org/10.1016/j.compstruct.2003.11.012>
4. Vel, S.S., Batra, R.C.: Exact solution for thermoelastic deformations of functionally graded thick rectangular plates. *AIAA J.* **40**(7), 1421–1433 (2002). <https://doi.org/10.2514/2.1805>
5. Vel, S.S., Batra, R.C.: Three-dimensional exact solution for the vibration of functionally graded rectangular plates. *J. Sound Vib.* **272**(3–5), 703–730 (2004). [https://doi.org/10.1016/S0022-460X\(03\)00412-7](https://doi.org/10.1016/S0022-460X(03)00412-7)
6. Matsunaga, H.: Free vibration and stability of functionally graded plates according to a 2D higher-order deformation theory. *Compos. Struct.* **82**(4), 499–512 (2008)
7. Nguyen-Xuan, H., Tran, L.V., Thai, C.H., Nguyen-Thoi, T.: Analysis of functionally graded plates by an efficient finite element method with node-based strain smoothing. *Thin Walled Struct.* **54**, 1–18 (2012). <https://doi.org/10.1016/j.tws.2012.01.013>
8. Mantari, J.L., Granados, E.V., Guedes Soares, C.: Vibrational analysis of advanced composite plates resting on elastic foundation. *Compos. B Eng.* **66**, 407–419 (2014)
9. Bellifa, H., Benrahou, K.H., Hadji, L., Houari, M.S.A., Tounsi, A.: Bending and free vibration analysis of functionally graded plates using a simple shear deformation theory and the concept the neutral surface position. *J. Braz. Soc. Mech. Sci. Eng.* **38**(1), 265–275 (2016). <https://doi.org/10.1007/s40430-015-0354-0>
10. Zaoui, F.Z., Ouinas, D., Tounsi, A.: New 2D and quasi-3D shear deformation theories for free vibration of functionally graded plates on elastic foundations. *Compos. B Eng.* **159**, 231–247 (2019)
11. Tati, A.: A five unknowns high order shear deformation finite element model for functionally graded plates bending behavior analysis. *J. Braz. Soc. Mech. Sci. Eng.* **43**(1), 1–14 (2021). <https://doi.org/10.1007/s40430-020-02736-1>
12. Tati, A.: Finite element analysis of thermal and mechanical buckling behavior of functionally graded plates. *Arch. Appl. Mech.* **91**, 4571–4587 (2021). <https://doi.org/10.1007/s00419-021-02025-w>

13. Sadgui, A., Tati, A.: A novel trigonometric shear deformation theory for the buckling and free vibration analysis of functionally graded plates. *Mech. Adv. Mater. Struct.* **29**, 6648–6663 (2021)
14. Belounar, A., Boussem, F., Houhou, M.N., Tati, A., Fortas, L.: Strain-based finite element formulation for the analysis of functionally graded plates. *Arch. Appl. Mech.* **92**(7), 2061–2079 (2022). <https://doi.org/10.1007/s00419-022-02160-y>
15. Belounar, A., Boussem, F., Tati, A.: A novel C0 strain-based finite element for free vibration and buckling analyses of functionally graded plates. *J. Vib. Eng. Technol.* **11**(1), 281–300 (2023). <https://doi.org/10.1007/s42417-022-00577-x>
16. Cuong, B.M., Tounsi, A., Thom, D.V., Van, N.T.H., Minh, P.V.: Finite element modelling for the static bending response of rotating FG-GPLRC beams with geometrical imperfections in thermal mediums. *Comput. Concr.* **33**(1), 91–102 (2024). <https://doi.org/10.12989/cac.2024.33.1.091>
17. Belabed, Z., Tounsi, A., Al-Osta, M., Tounsi, A., Minh, H.L.: On the elastic stability and free vibration responses of functionally graded porous beams resting on Winkler-Pasternak foundations via finite element computation. *Geomech. Eng.* **36**(2), 183–204 (2024). <https://doi.org/10.12989/gae.2024.36.2.183>
18. Belabed, Z., Tounsi, A., Bousahla, A.A., Tounsi, A., Yaylaci, M.: Accurate free and forced vibration behavior prediction of functionally graded sandwich beams with variable cross-section: a finite element assessment. *Mech. Based Des. Struct. Mach.* (2024). <https://doi.org/10.1080/15397734.2024.2337914>
19. Bentrar, H., Chorfi, S.M., Belalia, S.A., Tounsi, A., Ghazwani, M.H., Alnujaie, A.: Effect of porosity distribution on free vibration of functionally graded sandwich plate using the P-version of the finite element method. *Struct. Eng. Mech.* **88**(6), 551–567 (2023). <https://doi.org/10.12989/sem.2023.88.6.551>
20. Tien, D.M., Thom, D.V., Van, N.T.H., Tounsi, A., Minh, P.V., Mai, D.N.: Buckling and forced oscillation of organic nanoplates taking the structural drag coefficient into account. *Comput. Concr.* **32**(6), 553–565 (2023). <https://doi.org/10.12989/cac.2023.32.6.553>
21. Mesbah, A., Belabed, Z., Amara, K., Tounsi, A., Bousahla, A.A., Bourada, F.: Formulation and evaluation a finite element model for free vibration and buckling behaviors of functionally graded porous (FGP) beams. *Struct. Eng. Mech.* **86**(3), 291–309 (2023). <https://doi.org/10.12989/sem.2023.86.3.291>
22. Xia, L., Wang, R., Chen, G., Asemi, K., Tounsi, A.: The finite element method for dynamics of FG porous truncated conical panels reinforced with graphene platelets based on the 3-D elasticity. *Adv. Nano Res.* **14**(4), 375–389 (2023). <https://doi.org/10.12989/anr.2023.14.4.375>
23. Civalek, Ö., Uzun, B., Yayli, M.Ö.: A Fourier sine series solution of static and dynamic response of nano/micro-scaled FG rod under torsional effect. *Adv. NanoRes.* **12**(5), 467–482 (2022). <https://doi.org/10.12989/anr.2022.12.5.467>
24. Civalek, Ö., Uzun, B., Yayli, M.Ö.: Stability analysis of nanobeams placed in electromagnetic field using a finite element method. *Arab. J. Geosci.* **13**(21), 1165 (2020). <https://doi.org/10.1007/s12517-020-06188-8>
25. Civalek, Ö., Uzun, B., Yayli, M.Ö.: Frequency, bending and buckling loads of nanobeams with different cross sections. *Adv. Nano Res.* **9**(2), 91–104 (2020). <https://doi.org/10.12989/anr.2020.9.2.091>
26. Ebrahimi, F., Reza Barati, M.: Vibration analysis of nonlocal beams made of functionally graded material in thermal environment. *Eur. Phys. J. Plus.* **131**, 279 (2016). <https://doi.org/10.1140/epjp/i2016-16279-y>
27. Uzun, B., Yayli, M.Ö.: Rotary inertia effect on dynamic analysis of embedded FG porous nanobeams under deformable boundary conditions with the effect of neutral axis. *J. Braz. Soc. Mech. Sci. Eng.* **46**, 111 (2024). <https://doi.org/10.1007/s40430-023-04605-z>
28. Demir, Ç., Civalek, Ö.: A new nonlocal finite element method via Hermitian cubic shape functions for thermal vibration of nano beams surrounded by an elastic matrix. *Compos. Struct.* **168**, 872–884 (2017). <https://doi.org/10.1016/j.compstruct.2017.02.091>
29. Akgöz, B., Civalek, Ö.: Free vibration analysis of axially functionally graded tapered Bernoulli-Euler microbeams based on the modified couple stress theory. *Compos. Struct.* **98**, 314–322 (2013). <https://doi.org/10.1016/j.compstruct.2012.11.020>
30. Ashwell, D.G., Sabir, A.B.: A new cylindrical shell finite element based on simple independent strain functions. *Int. J. Mech. Sci.* **14**(3), 171–183 (1972)
31. Belarbi, M.T., Maalem, T.: On improved rectangular finite element for plane linear elasticity analysis. *Rev. Eur. Élém. Finis.* **14**(8), 985–997 (2012). <https://doi.org/10.3166/reef.14.985-997>
32. Rebiai, C., Belounar, L.: A new strain based rectangular finite element with drilling rotation for linear and nonlinear analysis. *Arch. Civ. Mech. Eng.* **13**, 72–81 (2013). <https://doi.org/10.1016/j.acme.2012.10.001>
33. Sabir, A.B.: A rectangular and triangular plane elasticity element with drilling degrees of freedom. In: Proceedings of the Second International Conference on Variational Methods in Engineering, vol. 9, pp. 17–25 (1985)
34. Belarbi, M.T., Charif, A.: Développement d'un nouvel élément hexaédrique simple basé sur le modèle en déformation pour l'étude des plaques minces et épaisses. *Rev. Eur. Élém. Finis.* **8**(2), 135–157 (1999)
35. Belounar, L., Guerraiche, K.: A new strain based brick element for plate bending. *Alex. Eng. J.* **53**, 95–105 (2014). <https://doi.org/10.1016/j.aej.2013.10.004>
36. Messai, A., Belounar, L., Merzouki, T.: Static and free vibration of plates with a strain based brick element. *Eur. J. Comput. Mech.* (2019). <https://doi.org/10.1080/17797179.2018.1560845>
37. Belounar, A., Benmebarek, S., Belounar, L.: Strain based triangular finite element for plate bending analysis. *Mech. Adv. Mater. Struct.* **27**(8), 620–632 (2020)
38. Belounar, A., Benmebarek, S., Houhou, M.N., Belounar, L.: Static, free vibration, and buckling analysis of plates using strain-based Reissner-Mindlin elements. *Int. J. Adv. Struct. Eng.* **11**, 211–230 (2019)
39. Belounar, A., Benmebarek, S., Houhou, M.N., Belounar, L.: Free vibration with Mindlin plate finite element based on the strain approach. *J. Inst. Eng. India Ser. C.* **101**, 331–346 (2020). <https://doi.org/10.1007/s40032-020-00555-w>
40. Belounar, L., Guenfoud, M.: A new rectangular finite element based on the strain approach for plate bending. *Thin Walled Struct.* **43**, 47–63 (2005). <https://doi.org/10.1016/j.tws.2004.08.003>
41. Boussem, F., Belounar, A., Belounar, L.: Assumed strain finite element for natural frequencies of bending plates. *World J. Eng.* **19**(5), 620–631 (2022)

42. Boussem, F., Belounar, L.: A plate bending Kirchhoff element based on assumed strain functions. *J. Solid Mech.* **12**(4), 935–952 (2020)
43. Djoudi, M., Bahai, H.: A shallow shell finite element for the linear and non-linear analysis of cylindrical shells. *Eng. Struct.* **25**, 769–778 (2003)
44. Sabir, A., Lock, A.: A curved, cylindrical shell, finite element. *Int. J. Mech. Sci.* **14**, 125–135 (1972)
45. Sabir, A., Mousa, A.: Finite-element analysis of cylindrical-conical storage tanks using strain-based elements. *Struct. Eng. Rev.* **4**, 367–374 (1996)
46. Reddy, J.N.: Mechanics of laminated composite plates and shells theory and analysis, 2nd edn. CRC Press, New York (2004)
47. Guenfoud, H., Himeur, M., Ziou, H., Guenfoud, M.: A consistent triangular thin flat shell finite element with drilling rotation based on the strain approach. *Int. J. Struct. Eng.* **9**, 191–223 (2018)
48. Fallah, A., Aghdam, M.M., Kargarnovin, M.H.: Free vibration analysis of moderately thick functionally graded plates on elastic foundation using the extended Kantorovich method. *Arch. Appl. Mech.* **83**, 177–191 (2013). <https://doi.org/10.1007/s00419-012-0645-1>
49. Barati, M.R.: Dynamic response of porous functionally graded material nanobeams subjected to moving nanoparticle based on nonlocal strain gradient theory. *Mater. Res. Express.* **4**(11), 115017 (2017). <https://doi.org/10.1088/2053-1591/aa9765>
50. Tati, A., Belounar, A., Sadgui, A.: Bending and free vibration analysis of FG circular plates using a five unknown high order shear deformation theory. *Mech. Based Des. Struct. Mach.* (2024). <https://doi.org/10.1080/15397734.2024.2315173>
51. Hirane, H., Belarbi, M.O., Houari, M.S.A., Tounsi, A.: On the layerwise finite element formulation for static and free vibration analysis of functionally graded sandwich plates. *Eng. Comput.* **38**(Suppl 5), 3871–3899 (2022). <https://doi.org/10.1007/s00366-020-01250-1>
52. Yin, S., Hale, J.S., Yu, T., Bui, T.Q., Bordas, S.P.A.: Isogeometric locking-free plate element: a simple first-order shear deformation theory for functionally graded plates. *Compos. Struct.* **118**, 121–138 (2014). <https://doi.org/10.1016/j.compstruct.2014.07.028>
53. Valizadeh, N., Natarajan, S., Gonzalez-Estrada, O.A., Rabczuk, T., Bui, T.Q., Bordas, S.P.A.: NURBS-based finite element analysis of functionally graded plates: static bending, vibration, buckling and flutter. *Compos. Struct.* **99**, 309–326 (2013). <https://doi.org/10.1016/j.compstruct.2012.11.008>
54. Thai, H.T., Choi, D.H.: A simple first-order shear deformation theory for the bending and free vibration analysis of functionally graded plates. *Compos. Struct.* **101**, 332–340 (2013)
55. Jin, G., Su, Z., Shi, S., Ye, T., Gao, S.: Three-dimensional exact solution for the free vibration of arbitrarily thick functionally graded rectangular plates with general boundary conditions. *Compos. Struct.* **108**, 565–577 (2014). <https://doi.org/10.1016/j.compstruct.2013.09.051>
56. Reddy, B.S., Kumar, J.S., Reddy, C.E., Reddy, K.V.K.: Buckling analysis of functionally graded material plates using higher order shear deformation theory. *J. Compos.* **2013**, 1–12 (2013). <https://doi.org/10.1155/2013/808764>
57. Thai, H.T., Choi, D.H.: An efficient and simple refined theory for buckling analysis of functionally graded plates. *Appl. Math. Model.* **36**(3), 1008–1022 (2012). <https://doi.org/10.1016/j.apm.2011.07.062>
58. Zenkour, A.M., Aljadani, M.H.: Mechanical buckling of functionally graded plates using a refined higher-order shear and normal deformation plate theory. *Adv. Aircr. Spacecr. Sci.* **5**(6), 615–632 (2018). <https://doi.org/10.12989/aas.2018.5.6.615>

Publisher's Note Springer Nature remains neutral with regard to jurisdictional claims in published maps and institutional affiliations.

Springer Nature or its licensor (e.g. a society or other partner) holds exclusive rights to this article under a publishing agreement with the author(s) or other rightsholder(s); author self-archiving of the accepted manuscript version of this article is solely governed by the terms of such publishing agreement and applicable law.